

Supplementary Information

Versatile Energy-Level-Tunable Hole-Transport Interlayer for Multi-Composition Inverted Perovskite Solar Cells

Wenbo Peng^{1,2†}, Yong Zhang^{1,2†*}, Xianyong Zhou^{3†}, Jiawen Wu^{1,2†}, Deng Wang^{1,2,4},
5 Geping Qu⁵, Jie Zeng^{1,2,4}, Yintai Xu^{1,6}, Bo Jiang^{1,2}, Peide Zhu^{1,2}, Yifan Du^{1,2}, Zhitong
Li¹, Xia Lei¹, Zhixin Liu^{1,2}, Lei Yan⁶, Xingzhu Wang^{1,2,3,7,8*}, and Baomin Xu^{1,2,9*}

¹Department of Materials Science and Engineering, Southern University of Science and Technology, Shenzhen 518055, China

10 ²Key University Laboratory of Highly Efficient Utilization of Solar Energy and Sustainable Development of Guangdong, Southern University of Science and Technology, Shenzhen 518055, China

³Engineering and Research Center for Integrated New Energy Photovoltaics & Energy Storage Systems of Hunan Province and School of Electrical Engineering, University
15 of South China, Hengyang 421001, China

⁴Department of Materials Science and Engineering, City University of Hong Kong, Kowloon 999077, Hong Kong

⁵Department of Chemistry, Southern University of Science and Technology, Shenzhen 518055, China

20 ⁶Department of Physics and Optoelectronic Engineering, Xiangtan University, Xiangtan 411100, China

⁷SUSTech Academy for Advanced Interdisciplinary Studies, Southern University of Science and Technology, Shenzhen 518055, China

⁸Shenzhen Putai Technology Co., Ltd., Longhua District, Shenzhen 518000, China

25 ⁹SUSTech Energy Institute for Carbon Neutrality, Southern University of Science and Technology, Shenzhen 518055, China

†These authors contributed equally to this work.

*Correspondence: zychem0@gmail.com (Yong Zhang)

*Correspondence: wangxz@sustech.edu.cn (Xingzhu Wang)

*Correspondence: xubm@sustech.edu.cn (Baomin Xu)

5

Experimental Section

Materials

All the solvents including *N, N*-dimethylformamide (DMF, 99.99%, J&K), dimethyl sulfoxide (DMSO, 99.9%, J&K), isopropanol (IPA, 99.5%, J&K), chlorobenzene (CB, 5 99.9%, J&K) were used as received without further purification. Nickel oxide nanoparticles (NiO_x , >99.999%) was bought from Advanced Election Technology CO., Ltd (China). Formamidinium iodide (FAI, >99.99%) and methylammonium iodide (MAI, >99.99%) were bought from greatcell solar materials Pty Ltd (Australia). Lead iodide (PbI_2 , >99.99%), lead bromide (PbBr_2 , >99.0%), [2-(9H-carbazol-9-yl) 10 ethyl] phosphonic acid (2PACz, >98.0%) and [4-(3,6-dimethyl-9H-carbazole-9-yl) butyl] phosphonic acid (Me-4PACz, >99.0%) were bought from TCI (Japan). Cesium iodide (CsI, 99.999%), methylammonium chloride (MAcI, 99.5%), [4-(3,6-dibromo-9H-carbazole-9-yl) butyl] phosphonic acid (Br-4PACz, 99.0%), piperazine hydroiodide (PI, 99.5%), bathocuproine (BCP, 99%) and [60]Fullerene (C_{60} , 99%) were bought 15 from Xi'an Yuri Solar Co., Ltd (China).

Perovskite precursor preparation

Anti-solvent perovskite: 1.63 M reference perovskite precursor solutions were constructed by mixing CsI, FAI, MAI, PbI_2 , in DMF: DMSO mixed solvent (4:1/v:v) with a chemical formula of $\text{Cs}_{0.05}\text{FA}_{0.85}\text{MA}_{0.1}\text{PbI}_3$.

20 Anti-solvent-free perovskite: 2.0 M reference perovskite precursor solutions were constructed by mixing CsI, FAI, PbI_2 , in DMF: NMP mixed solvent (5:1/v:v) with a

chemical formula of $\text{Cs}_{0.17}\text{FA}_{0.83}\text{PbI}_3$.

Wide-bandgap perovskite: 1.2 M reference perovskite precursor solutions were constructed by mixing CsI, FAI, PbI_2 , PbBr_2 , in DMF: DMSO mixed solvent (3:1/v:v) with a chemical formula of $\text{Cs}_{0.2}\text{FA}_{0.8}\text{PbI}_{1.5}\text{Br}_{1.5}$.

- 5 For completely dissolution, the prepared precursor solutions should be oscillating stirring for over 2 hours. After oscillating stirring to transparent, the solution was filtered through 0.22 μm PTFE filter, and then stored at room temperature.

Device fabrication

- The patterned ITO and FTO glass (10 Ω/sq , 1.5 \times 1.5 cm) was washed by sonication with
- 10 diluted wash buffer, deionized water, and isopropanol for 30 min each. Then, the ITO glasses were cleaned by a UV-ozone cleaner for 30 min. 60 μl NiO_x solution (10 mg/ml, filtered through 0.22 μm PES filter) was spin-coated at 1000 rpm for 1 s and 3000 rpm for 40 s as HTL. The HTL-coated substrates were heated to 110 $^\circ\text{C}$ for 15 min in N_2 atmosphere to accelerate the formation of NiO_x dry film. 1 mmol/L SAM solution (Me-
 - 15 4PACz dissolved in IPA, Br-4PACz dissolved in IPA: methanol = 3: 1) was subsequently spin-coated onto the NiO_x film at 5000 rpm for 30 s, followed by heating at 100 $^\circ\text{C}$ for 10 min.

- 60 μl perovskite solution was subsequently deposited on NiO_x/SAM substrate. For anti-solvent perovskite, 60 μl perovskite solution was spin-coated at 1000 rpm for 10 s and
- 20 5000 rpm for 30 s with the assistance of antisolvent (CB) at the last 12 s. Then, the perovskite films were annealed at 100 $^\circ\text{C}$ for 30 min. For anti-solvent-free perovskite,

60 μl perovskite solution was spin-coated at 5000 rpm for 40 s. Then, the perovskite films were annealed at 150°C for 10 min. For wide-bandgap perovskite, 60 μl perovskite solution was spin-coated at 1000 rpm for 2 s and 3000 rpm for 40 s with the assistance of antisolvent (CB) at the last 20 s. Then, the perovskite films were annealed
5 at 100°C for 15 min.

60 μl PI solution (dissolved in IPA) with a concentration of 0.5 mg/ml was subsequently spin-coated onto the perovskite layer at 5000 rpm for 30 s as a passivation layer, followed by a heating process at 100°C for 5 min. Subsequently, 30 nm of C_{60} , 8 nm of BCP and 100 nm of copper was thermally evaporated under vacuum of 4×10^{-5} Torr at
10 the evaporation rate of 0.2 $\text{\AA}/\text{s}$. Finally, 100 nm MgF_2 was thermally evaporated on the quartz glass side of the device under vacuum of 4×10^{-5} Torr at the evaporation rate of 0.8 $\text{\AA}/\text{s}$ as antireflection layer.

Characterizations

UPS characterizations were conducted in a VG ESCALAB 220i-XL surface analysis
15 system equipped with a Hedischarge lamp ($h\nu = 21.22$ eV) and a monochromatic $\text{Al-K}\alpha$ X-ray gun ($h\nu = 1486.6$ eV), respectively. The binding energy of the UPS spectra was calibrated with a 5 V bias voltage, the work function was calculated by $E_{WF} = 21.2 - E_{cut-off}$, and the HOMO level was calculated by $|E_{HOMO}| = |E_{WF}| + |E_{VBM}|$.
The XPS was measured by Escalab Xi^+ X-ray photoelectron spectroscopy. Kelvin
20 probe force microscopy (KPFM) data were carried out by the atomic force microscopy (Bruker Dimension ICON) using MESP probe with a scanning frequency of 1Hz under

indoor lighting conditions. The UV-vis (ultraviolet-visible) absorption spectra of the films were acquired by using the spectrophotometer (Perkin Elmer Lambda 950). The morphology of samples was observed by a field-emission scanning electron microscope (SEM) and energy-dispersive X-ray spectroscopy (EDS) (SU8230, Hitachi). The X-ray 5 diffraction (XRD) spectra were measured with an D8 Advance ECO X-ray Diffractometer using Cu K α radiation under operating conditions of 25 kV and 15 mA from 5° to 50°. The Grazing-incidence wide-angle X-ray scattering (GIWAXS) measurements were conducted at the Synchrotron Light Source in Shanghai (BL14B1 beamline). Atomic force microscope (AFM) measurements were conducted using 10 Bruker Dimension Edge under tapping mode. The steady-state photoluminescence (PL) spectra were taken on an FLS980 (Edinburgh Instruments Ltd.), equipped with a Xe lamp. Time-resolved photoluminescence (TRPL) decay transients were measured at 796 nm using excitation with a 450.5 nm light pulse from an Edinburgh FLS980 fluorimeter.

15 Device performance was characterized by a Keithley 2400 source meter and a Newport solar simulator (Enlitech Solar Simulator SS-F7-3A, xenon lamp) which offered the simulated AM 1.5G illumination of 100 mW cm⁻² in nitrogen glove box at room temperature without encapsulation using a shadow mask. Calibration was done using a NIST-certified monocrystalline Si solar cell (Newport 532 ISO1599). The *J-V* curves 20 were obtained from forward scans (-0.1 V to 1.2 V for anti-solvent PSCs and anti-solvent-free PSCs, -0.1 V to 1.36 V for wide-bandgap PSCs) and reverse scans (1.2 V to -0.1 V for anti-solvent PSCs and anti-solvent-free PSCs, 1.36 V to -0.1 V for wide-

bandgap PSCs) with a voltage step of 0.01 V and a delay time of 1 ms. No precondition was conducted in device measurements. Each device has an active area of 0.1 cm² and was measured unencapsulated using a shadow mask of 0.0736 cm² aperture area. The EQE was measured by a DSR100UV-B spectrometer with an SR830 lock-in amplifier.

5 The transient photovoltage decay (TPV) and transient photocurrent (TPC) were obtained by transient photoelectric streamer voltage measurement system (SouthPort SP-TPVC).

Device stability Measurements

The operational stability tests were carried out at the maximum power point (MPP) for
10 the unencapsulated cells under AM 1.5G 1 sun continuous illumination in nitrogen (N₂) atmosphere which was produced by a LED-lamp-based solar simulator. The bias at the MPP was calculated and applied automatically. The light intensity was calibrated by a standard silicon reference cell from Newport.

Supplementary Note

15 1. TRPL, TPV and TPC decay curve fitting

The decay curve fitting of TPV and TPC follows the single-exponential equation (1):

$$y = y_0 + A_1 e^{-x/\tau_1} \quad (1)$$

The decay curve fitting of TRPL follows the bi-exponential equation (2):

$$y = y_0 + A_1 e^{-x/\tau_1} + A_2 e^{-x/\tau_2} \quad (2)$$

20 The average lifespan can be calculated via equation (3) shown as follow:

$$\tau_{avg} = \frac{(A_1\tau_1^2 + A_2\tau_2^2)}{A_1\tau_1 + A_2\tau_2} \quad (3)$$

where A_1 and A_2 are the correlation coefficient of carrier lifetime τ_1 and τ_2 , respectively.

2. Trap density calculation based on SCLC measurement

With a hole-only structure of ITO/NiO_x/(SAM)/perovskite/PTAA/Au, the trap density (N_{trap}) could be quantitatively determined by following equation (4):¹

$$N_{trap} = \frac{2\varepsilon_0\varepsilon V_{TFL}}{qd^2} \quad (4)$$

where ε_0 is the vacuum permittivity (8.854×10^{-12} F/cm), ε is the dielectric constant of perovskite, V_{TFL} is the trap-filling limit voltage extracted from SCLC measurement, q is the elementary charge (1.602×10^{-19} C), d is the thickness of perovskite film. The dielectric constant can be estimated from impedance measurement using equation (5):

$$\varepsilon = Cd/A\varepsilon_0 \quad (5)$$

where C is the capacitance at high frequency ($\sim 10^4$ Hz), d is the thickness of perovskite, A active area (0.1 cm^2), and ε_0 is the vacuum permittivity (8.854×10^{-12} F/cm).

3. DFT calculations

The geometry optimizations for bulk, slabs, surface adsorptions, molecular used the VASP code with a plane wave (PW) basis set and projected augmented wave (PAW) pseudopotentials (PPs).² We employed the spin-polarized PBE flavor of the GGA PPs, and long-range dispersion interactions were considered by the DFTD3 scheme. The kinetic energy cut-off is 500 eV for the expansion of the wavefunctions. The convergence thresholds were set to 10^{-6} eV for energy and $0.05 \text{ eV } \text{\AA}^{-1}$ for the norm of

the atomic forces.

The cell parameters for cubic NiO were optimized with a $6 \times 6 \times 6$ mesh centered at the Gamma point, respectively. The optimized parameters are $a = b = c = 4.22 \text{ \AA}$, and $\alpha = \beta = \gamma = 90^\circ$ for NiO. We performed the adsorption calculations on the (100) surface of the perovskite and NiO, based on a $5 \times 5 \times 2$ NiO slab, respectively. The ionic optimizations fixed the bottom two atom layers to represent the bulk structures. We added a 12 \AA vacuum space to the perovskite and NiO slabs to avoid artificial interactions between the neighboring cells. Dipole corrections are applied to the z-direction to eliminate the artificial electrostatic interactions between the asymmetric repeated slabs. The Hubbard corrections, $U = 8 \text{ eV}$ and $J = 0.95 \text{ eV}$ were used for Ni to account for the strong electron correlations in 3d orbitals.³ All adsorption calculations were done at the gamma point. The adsorption energy (ΔE_{ads}) is defined as:

$$\Delta E_{ads} = E_{slab + molecule} - E_{slab} - E_{molecule}$$

4. SCAPS-1D simulation

According to previous research, simulations related to perovskite structures were conducted using the Solar Cell Capacitance Simulator in One dimension (SCAPS-1D) (version 3.3.10).^{4,6} Due to the nature of the calculation based on multiple formulas, several situations are approximated as ideal states or ignored during the calculation process. Three limitations have significant impact on the results: the source of parameters for the corresponding materials, the set ambient temperature, and the number of data measurements.⁴ The simulations including in this study were all

performed under the environmental parameters listed in the **Table S2**, with the AM 1.5G solar spectrum (100 mW cm⁻²) employed as the simulated solar light source.

The simulation results of SCAPS-1D are primarily based on the following three differential equations:

$$5 \quad \frac{\partial}{\partial x} \left(\epsilon_0 \epsilon \frac{\partial \Psi}{\partial x} \right) = -q(p - n + N_D^+ - N_A^- + N_{def}) \quad (6)$$

$$-\frac{\partial J_n}{\partial x} - U_n + G = \frac{\partial n}{\partial x} \quad (7)$$

$$-\frac{\partial J_p}{\partial x} - U_p + G = \frac{\partial p}{\partial x} \quad (8)$$

Here, ϵ_0 is the vacuum permittivity (8.8542×10⁻¹⁴ F/cm), ϵ is the relative permittivity, Ψ is the electrostatic potential, q is the elementary charge (1.602×10⁻¹⁹ C), n (p) is the electron (hole) density, N_D^+ (N_A^-) is the density of ionized donors (acceptors), N_{def} is the possible defect density, J_n (J_p) is the electron (hole) current densities, U_n (U_p) is the net electron (hole) recombination rate, G is the electron-hole generation rate.

The electron and hole density are given by:

$$J_n = qn\mu_n E + qD_n \frac{\partial n}{\partial x} \quad (9)$$

$$15 \quad J_p = qp\mu_p E - qD_p \frac{\partial p}{\partial x} \quad (10)$$

Where μ_n (μ_p) is the electron (hole) mobility, and D_n (D_p) is the diffusion coefficient of the electron (hole).

To gain a thorough understanding of the role of band structure played in the device, it is necessary to introduce a tunable interlayer. We introduced a SAM passivation layer 20 with a thickness of 5 nm between NiO_x and perovskite. Due to the ultra-thin structure of the SAM interlayer, we assume that the SAM passivation layer does not introduce additional interface losses. According to the definition of electron affinity, $E = |E_c|$, E_c

is the conduction band energy. Therefore, in the simulation process, we adjusted the band structure by varying the values of the bandgap and electron affinity of the SAM passivation layer, enabling simulations of devices with different band structures. The device band structures and carrier densities shown in **Figure 2b-e** were obtained at a 5 0V bias simulation, while the device efficiency in **Figure 2f** was simulated by applying a positive bias of 0 to 1.2V. Interface losses were set between NiO_x and PVK, with interface defects set $1 \times 10^{12} \text{ cm}^{-2}$ for **Figure 2b-e** and a range of $1 \times 10^{11} \text{ cm}^{-2}$ to $1 \times 10^{13} \text{ cm}^{-2}$ for **Figure 2f**. Other parameters related to simulation are listed in **Tables S3** and **S4**.

10 **5. Mott-Schottky plots**

The capacitance-voltage (*C-V*) curve of PSCs in the Mott-Schottky configuration are carried out to investigate the interfacial carrier density and the calculation formula is as follows:

$$\frac{1}{C^2} = \frac{2(V_{bi} - V)}{A^2 q \epsilon_0 \epsilon N_A} \quad (11)$$

15 where V_{bi} is the built-in potential, V is the applied voltage, A is the device active area (0.1 cm^2), N_A is the doping concentration, q is the elementary charge, ϵ is dielectric constant, ϵ_0 is the vacuum permittivity.

6. Calculation of quasi-Fermi level splitting (QFLS) and V_{oc-imp}

The calculation of QFLS and V_{oc-imp} is determined according to Neher et al.⁷ and Tan et al..⁸ The ‘implied V_{OC} ’ (V_{oc-imp}) of perovskite/charge-selective contacts

heterojunctions was evaluated following the equation: $V_{OC-imp} = QFLS/q$, where q is the elementary charge. The QFLS of PSCs consists of two parts. Based on the assumption that all PL emission comes from the radiative recombination of free charges in perovskite film, the PL quantum yield (PLQY) has a direct relationship to the QFLS, as shown in equation (12), and the ‘implied V_{OC} ’ nonradiative recombination ($\Delta V_{OC-imp}^{nonrad}$) can be calculated by equation (13):

$$QFLS = QFLS_{rad} + k_B T \ln(PLQY) = k_B T \ln\left(\frac{J_G}{J_{0,rad}}\right) + k_B T \ln\left(\frac{J_{rad}}{J_{rad} + J_{nonrad}}\right) \quad (12)$$

$$\Delta V_{OC-imp}^{nonrad} = \frac{QFLS_{rad} - QFLS}{q} = -\frac{k_B T \ln(PLQY)}{q} \quad (13)$$

where q is the elementary charge, $QFLS_{rad}$ is the QFLS for the perovskite layer when only radiative recombination is present, k_B is the Boltzmann’s constant (1.38×10^{-23} J/K), T is the room temperature (300 K), $k_B T \ln(PLQY)$ is the QFLS loss caused by the nonradiative recombination, J_G is the generation current density under illumination, and $J_{0,rad}$ is the dark radiative recombination saturation current density. The PLQY was conducted an FLS980 (Edinburgh Instruments Ltd.) by a 450.5 nm laser taken from the bottom ITO side inside an integrated sphere (**Figure S40**).

According to the detailed balance theory, the $J_{0,rad}$ can be calculated by the following equations:

$$J_{0,rad} = q \int_0^{\infty} EQE_{PV}(E) \phi_{BB}(E) dE \quad (14)$$

$$\phi_{BB}(E) = \frac{2\pi E^2}{h^3 c^2} \frac{1}{\exp\left(\frac{E}{k_B T}\right) - 1} \quad (15)$$

where q is the elementary charge, EQE_{PV} is the photovoltaic external quantum

efficiency, ϕ_{BB} is the black-body radiative spectrum, E is the photo energy, h is the Planck constant (6.626×10^{-34} J·s), and c is the light speed in vacuum (2.997×10^8 m/s). $J_{0,rad}$ of inverted PSCs with NiO_x and ET-HTL-10% is evaluated by EQE curves measured in **Figure S31a**, which was calculated as 1.73×10^{-20} mA cm⁻² for the NiO_x device and 2.05×10^{-20} mA cm⁻² for the ET-HTL-10% device, respectively. J_G is approximated to the J_{SC} of devices in this case. Therefore, the Q^{FLS}_{rad} of two kinds of devices was determined as 1.259 eV for the NiO_x device and 1.255 eV for the ET-HTL-10% device, respectively. The identical Q^{FLS}_{rad} value indicates the negligible difference of radiative recombination loss for two kinds of devices, which is mainly caused by perovskite films. Finally, the QFLS and $\Delta V_{oc-imp}^{nonrad}$ of HTL/perovskite and HTL/perovskite/ETL junctions can be determined (**Figure 5e** and **Figure S41**).

7. Trap density of states (tDOS) calculation

Thermal admittance spectroscopy was carried out in a Dielectric Temperature Spectrum Measuring System (DMS-2000) equipped with a precision LCR Meter (Keysight E4980A). at 0 V bias in dark area and a tuned frequency range from 1 Hz to 2×10^6 Hz.

The attempt-to-escape frequency was chosen to be 1×10^{12} Hz.

The significant profile of trap density of states (tDOS) is deduced from the angular frequency-dependent capacitance by following equation (16) and (17):

$$DOS(E_\omega) = -\frac{V_{bi} dC}{qWd\omega k_B T} \omega \quad (16)$$

$$\omega = 2\pi f \quad (17)$$

where C is the capacitance, ω is the angular frequency, f is the tuned frequency, q is the elementary charge, k_B is the Boltzmann's constant and T is the temperature, V_{bi} and W are the built-in potential and depletion width, respectively, which were extracted from the Mott-Schottky analysis shown in **Figure 5b**.

5 The depletion width W can be calculated at 0 V bias:

$$W = \sqrt{\frac{2\varepsilon_0\varepsilon V_{bi}}{qN_A}} \quad (18)$$

where ε_0 is the vacuum permittivity (8.8542×10^{-14} F/cm), ε is the dielectric constant of perovskite, N_A is the doping concentration.

The applied angular frequency ω defines an energetic demarcation:

$$10 \quad E_\omega = k_B T \ln\left(\frac{\omega_0}{\omega}\right) \quad (19)$$

where ω_0 is the attempt-to-escape frequency.

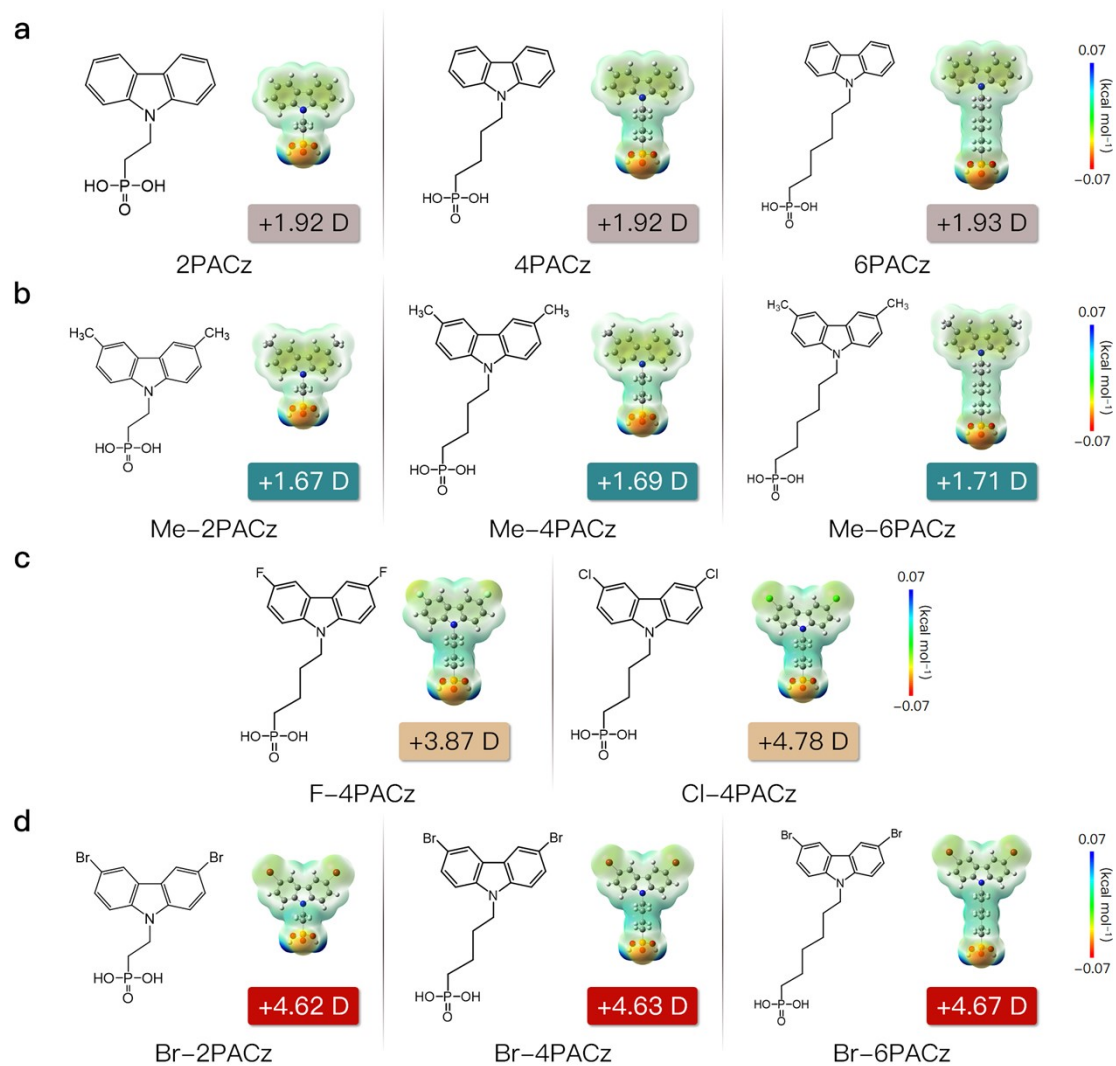


Figure S1. The molecular structures of SAMs with different spacer lengths (n), functional groups, and their corresponding dipole moments, electrostatic potential (ϕ) calculated via DFT method. The calculation processes were carried out using “Gaussian 5 16W” software with the B3LYP exchange-correlation functional.

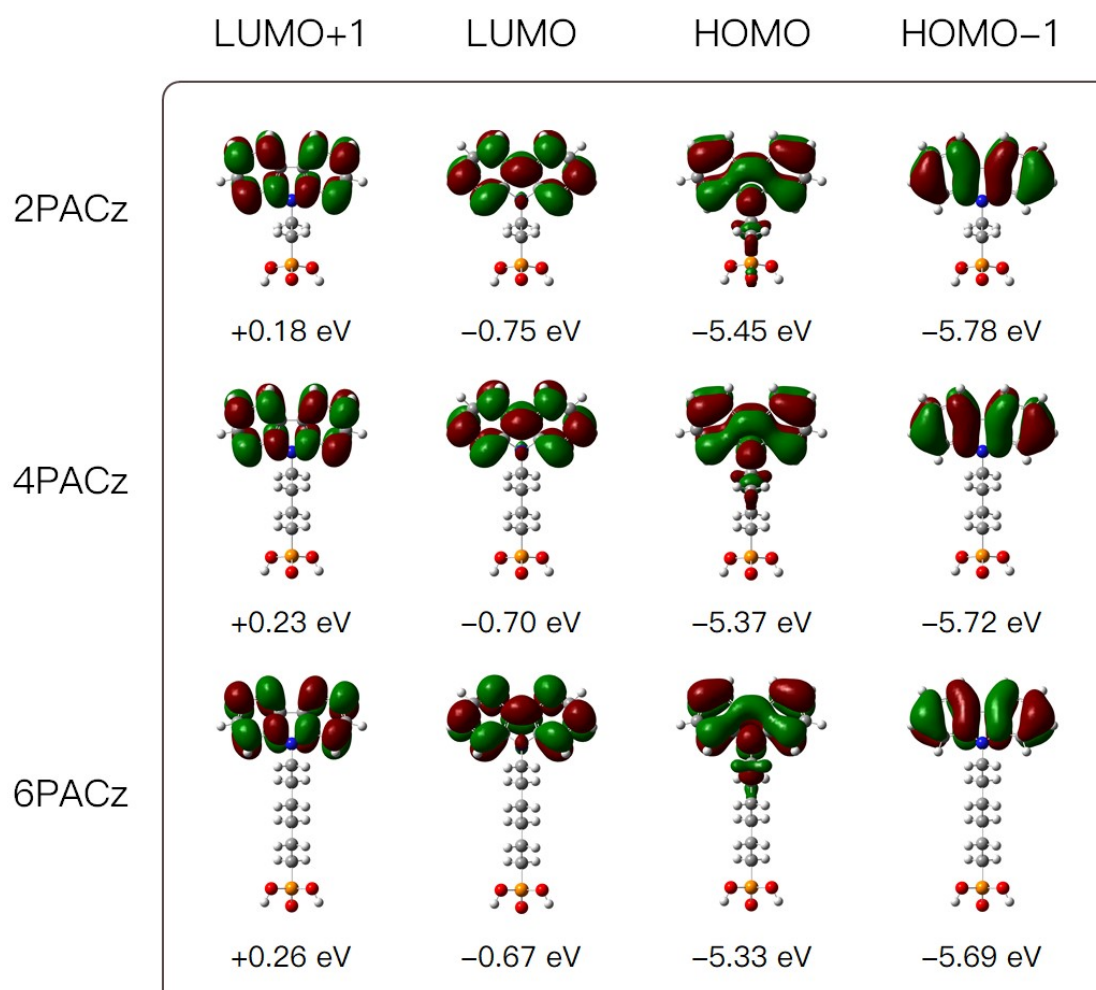


Figure S2. Calculation results of the HOMO, LUMO and neighboring energy levels of n PACz with different spacer lengths. The calculation results were further refined using B3LYP single point energy calculations based on the results in **Figure S1**.

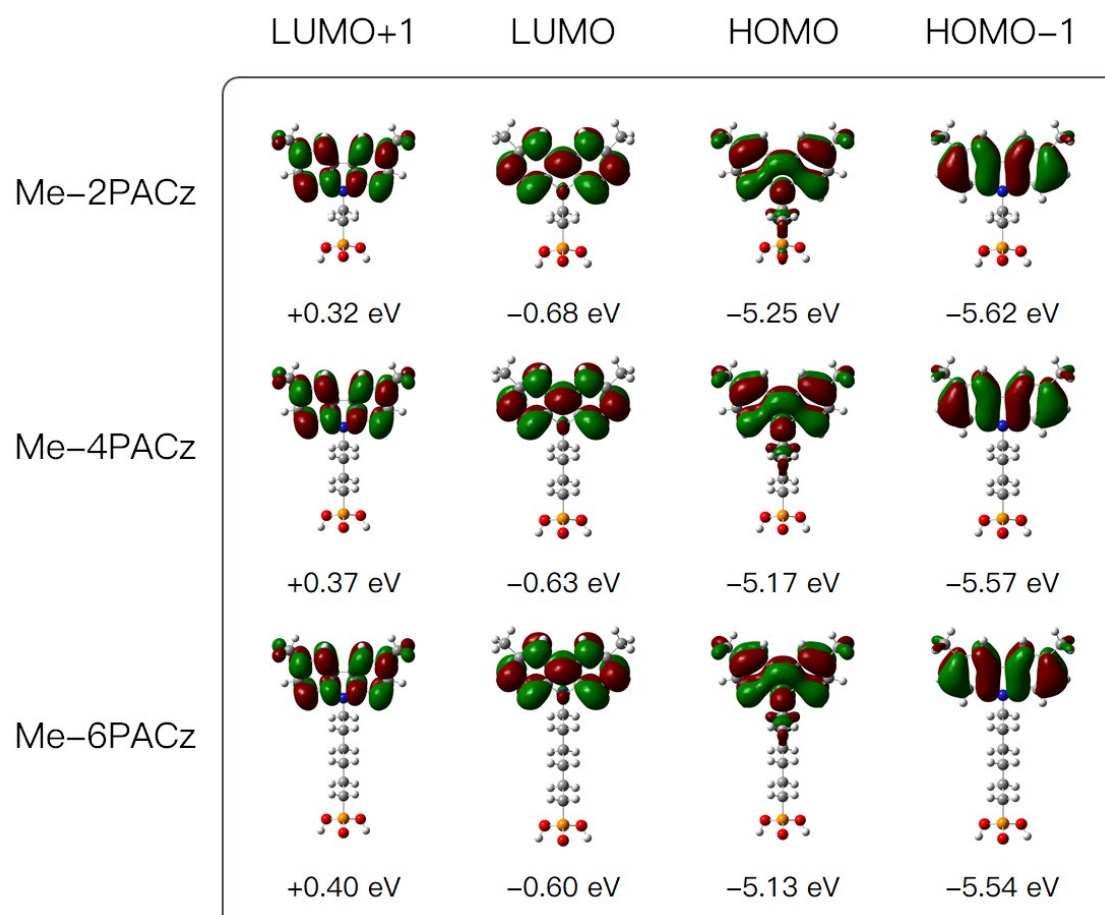


Figure S3. Calculation results of the HOMO, LUMO and neighboring energy levels of Me-*n*PACz with different spacer lengths. The calculation results were further refined using B3LYP single point energy calculations based on the results in **Figure S1**.

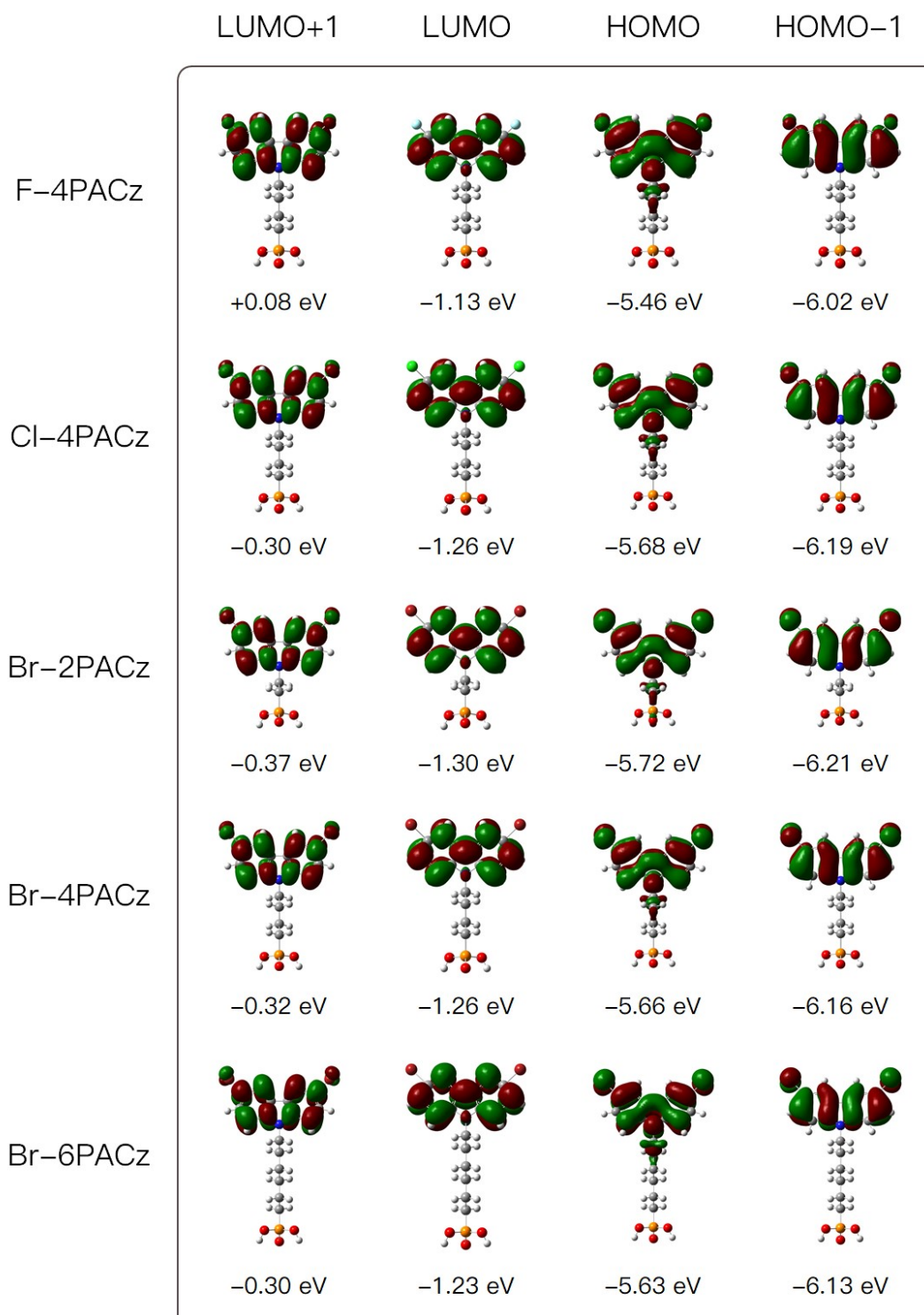


Figure S4. Calculation results of the HOMO, LUMO and neighboring energy levels of halogen-*n*PACz with different spacer lengths and functional groups. The calculation results were further refined using B3LYP single point energy calculations based on the

5 results in **Figure S1**.

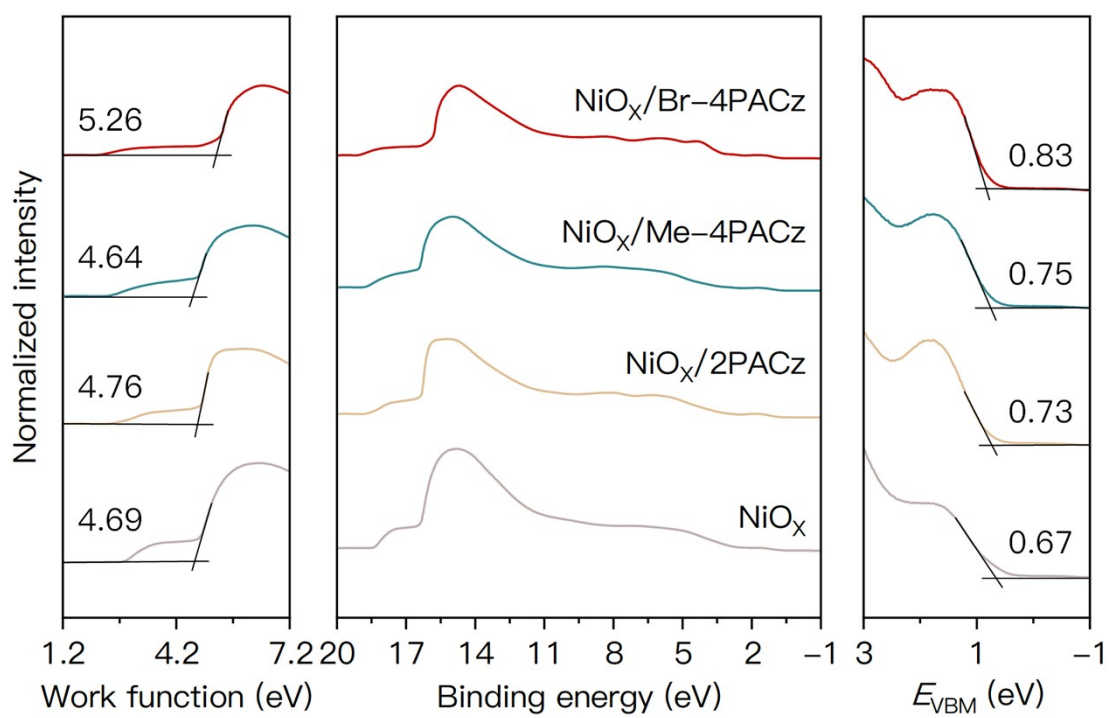


Figure S5. The UPS spectra, calculated work function and E_{VBM} values of bare NiO_x and NiO_x modified by 2PACz, Me-4PACz and Br-4PACz.

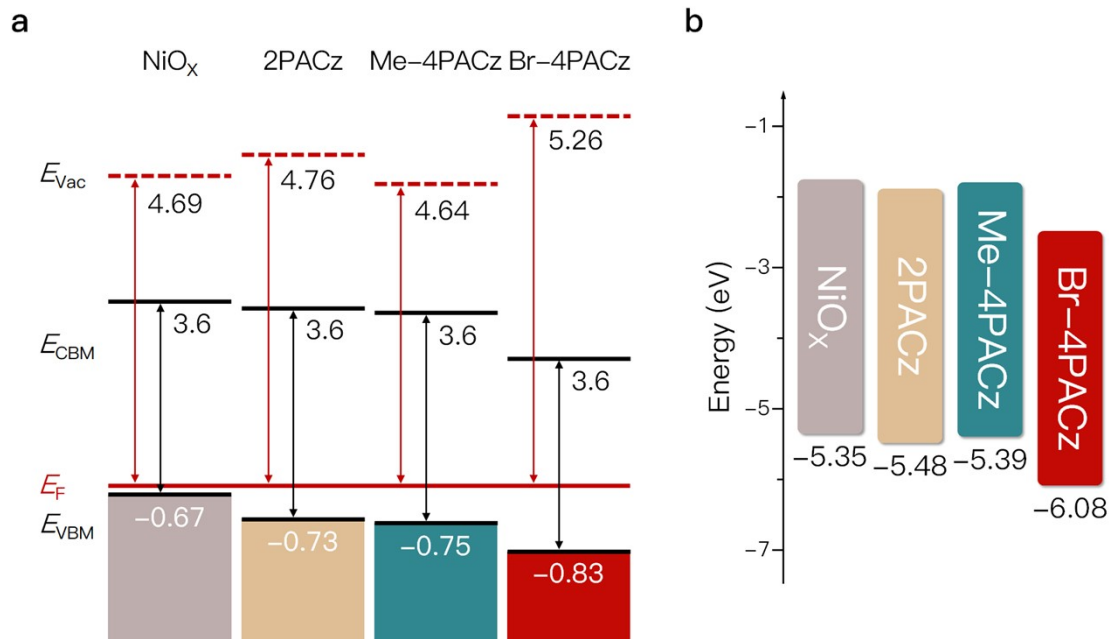


Figure S6. (a) Summarized energy level diagram of NiO_x and NiO_x modified by 2PACz, Me-4PACz and Br-4PACz in reference of Fermi level (E_F), including work function, E_{VBM} and E_{CBM} . (b) Band structure diagram of NiO_x, NiO_x/2PACz, NiO_x/Me-4PACz and NiO_x/Br-4PACz in reference of vacuum level, including HOMO level and LUMO level. The corresponding values were determined from UPS measurement results in **Figure S5**.

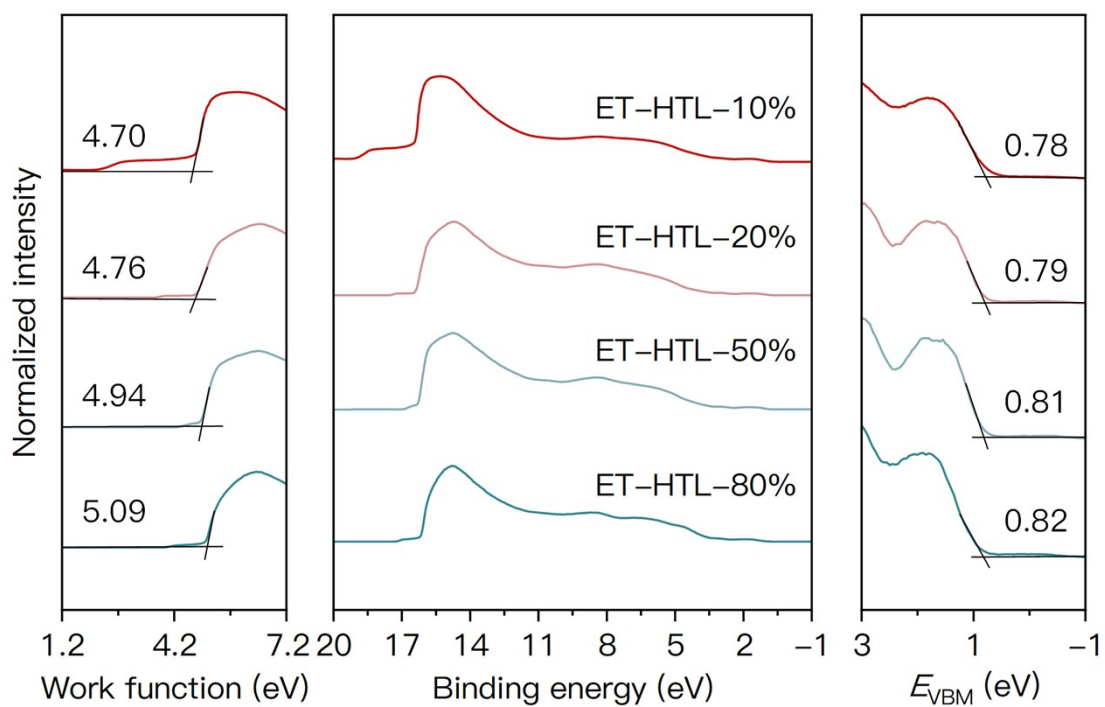


Figure S7. The UPS spectra, calculated work function and E_{VBM} values of ET-HTL with different Br-4PACz molar ratios.

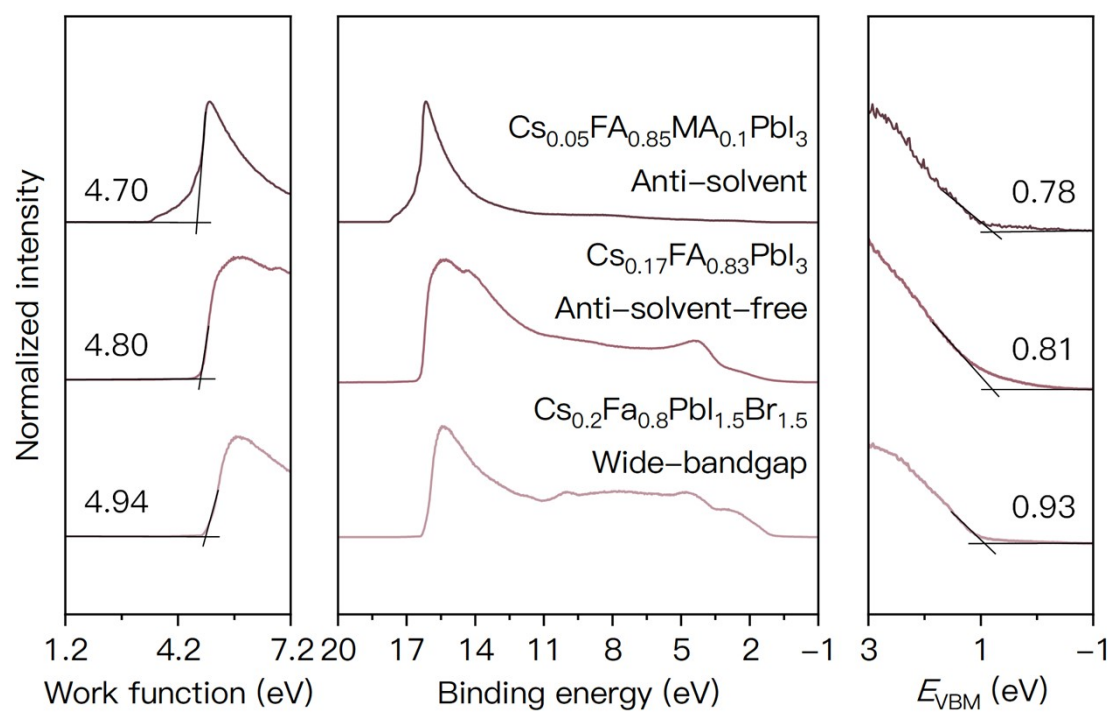


Figure S8. The UPS spectra, calculated work function and E_{VBM} values of perovskite films with different compositions including anti-solvent perovskite, anti-solvent-free perovskite and wide-bandgap perovskite.

5

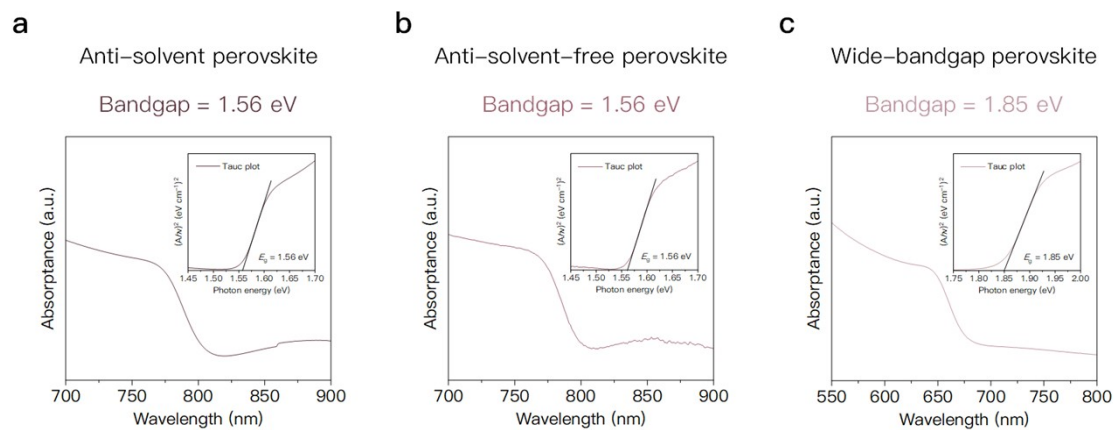


Figure S9. The UV absorption spectra and corresponding tauc plots of perovskite films with different compositions including (a) anti-solvent perovskite, (b) anti-solvent-free perovskite and (c) wide-bandgap perovskite.

5

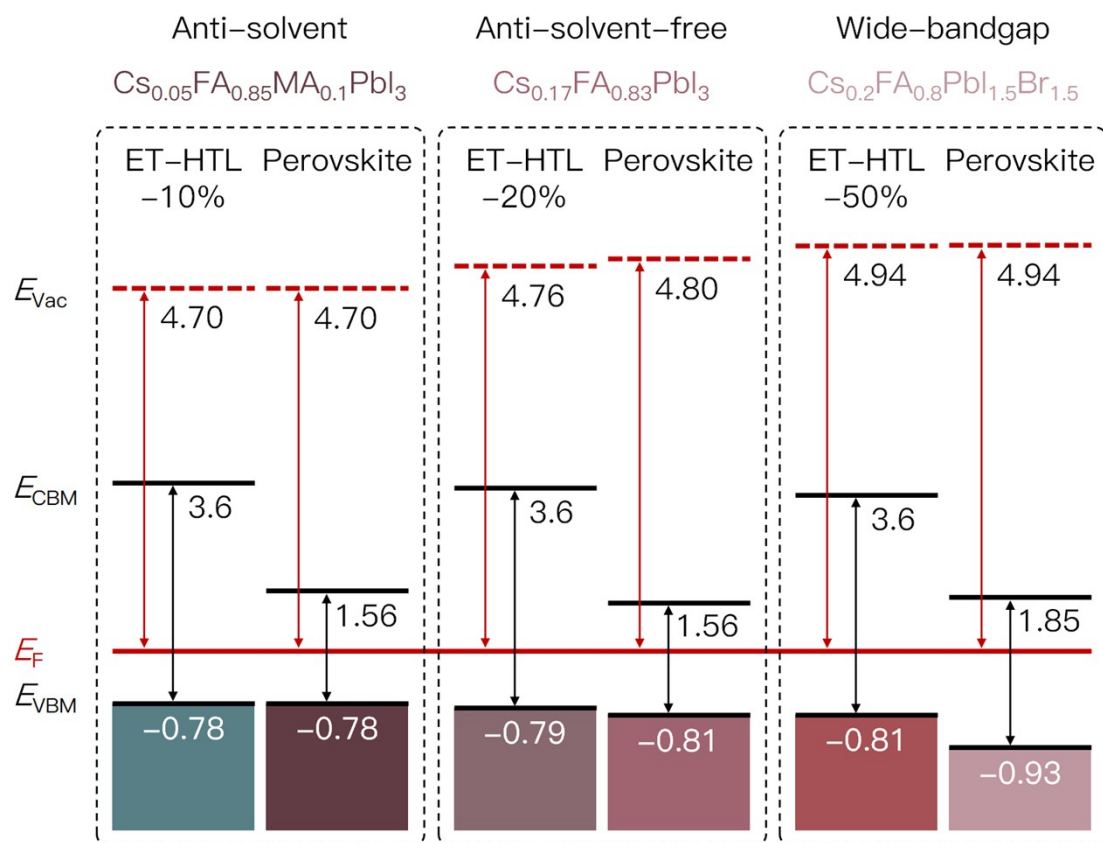


Figure S10. Summarized energy level diagram of different perovskite compositions and corresponding energy-matched ET-HTLs in reference of Fermi level (E_F), including work function, E_{VBM} and E_{CBM} .

5

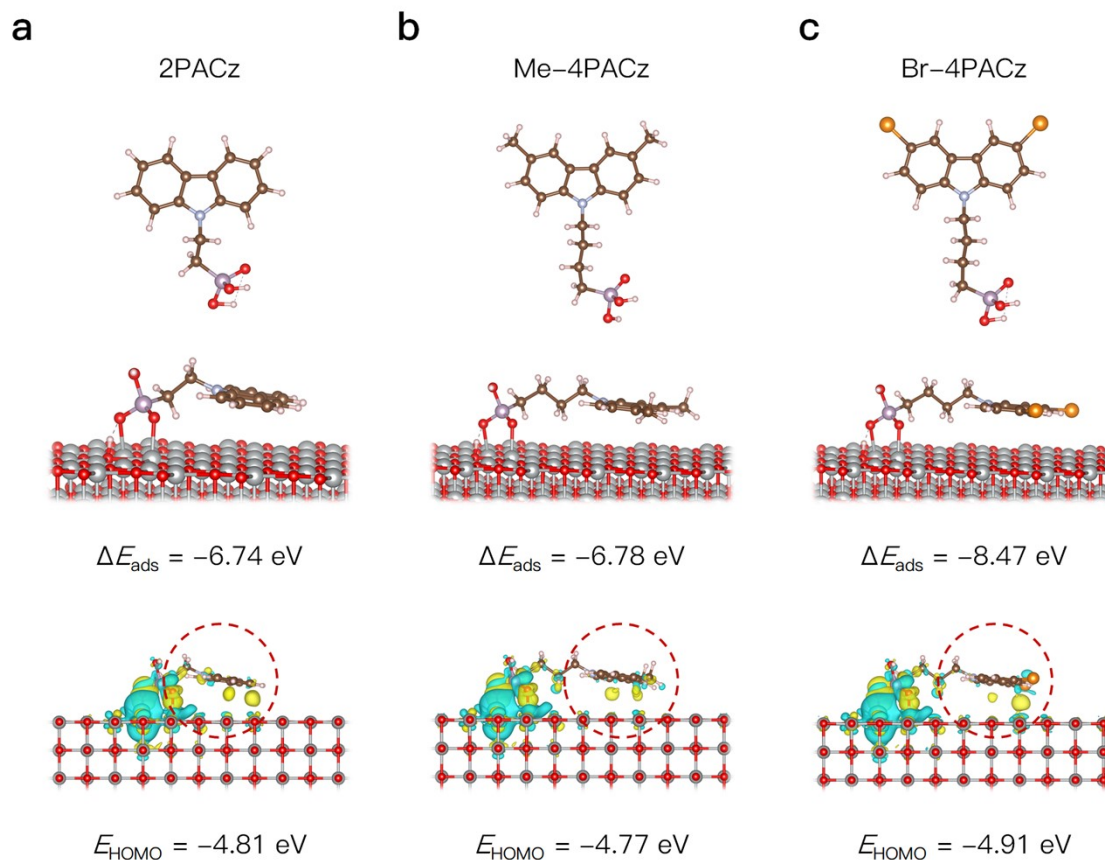


Figure S11. Molecule structure, assembly model and corresponding differential charge densities between NiO and (a) 2PACz, (b) Me-4PACz and (c) Br-4PACz using DFT calculation method, with demonstration of corresponding adsorption energy (ΔE_{ads}) and HOMO level of each SAM after bonding with NiO.

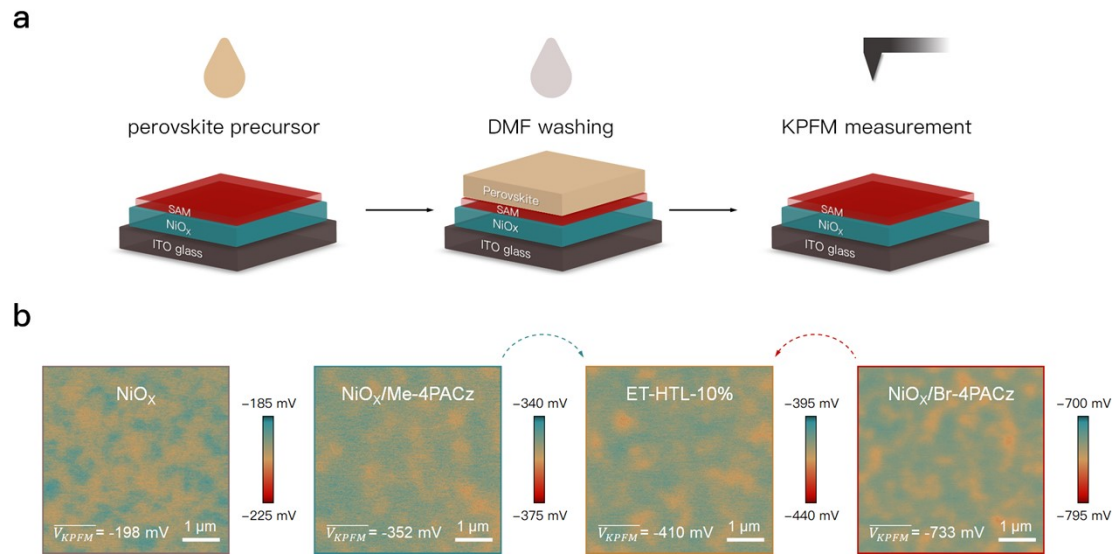


Figure S12. (a) Schematic diagram of DMF post-washing method for buried interface KPFM measurement. (b) KPFM measurement and surface potential results of corresponding hole-transport substrates after perovskite deposition.

5

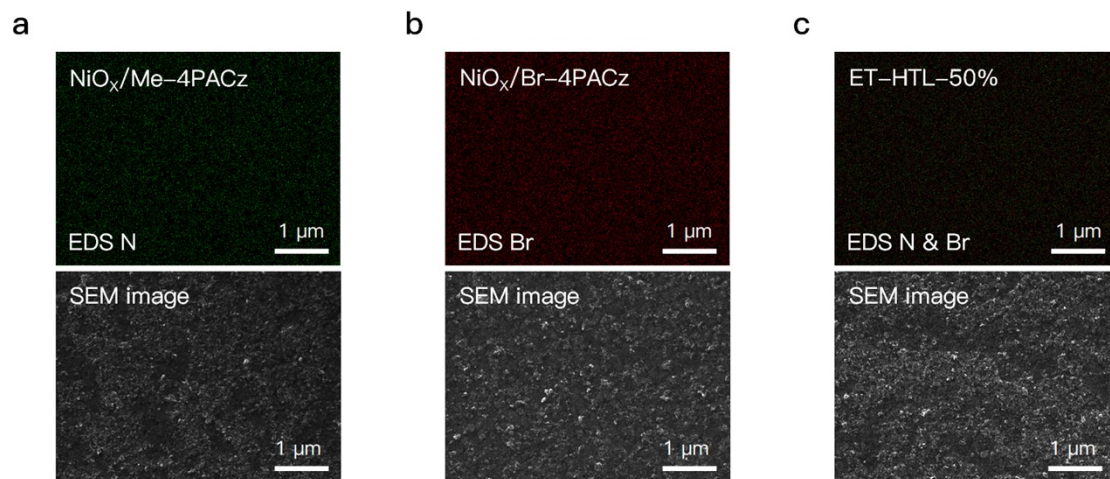


Figure S13. EDS measurement results and corresponding SEM images of NiO_x film modified by (a) Me-4PACz, (b) Br-4PACz and (c) ET-HTL-50%. The green signal represents the N in Me-4PACz, and the red signal represents the Br in Br-4PACz.

5

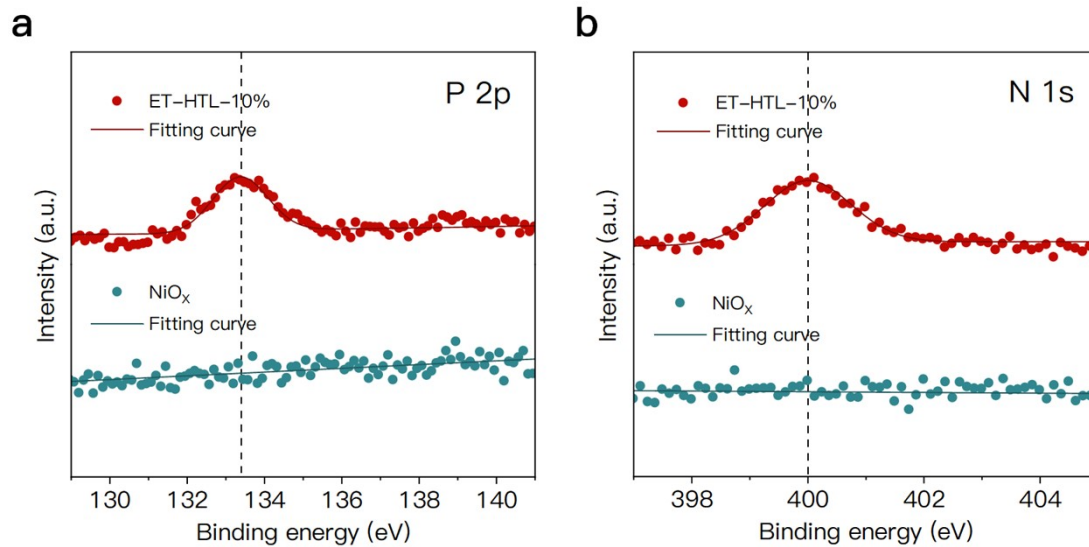


Figure S14. The XPS spectra of (a) P 2p and (b) N 1s of bare NiO_x and ET-HTL-10%.

The results have been calibrated using standard carbon (C) peak (284.80 eV).

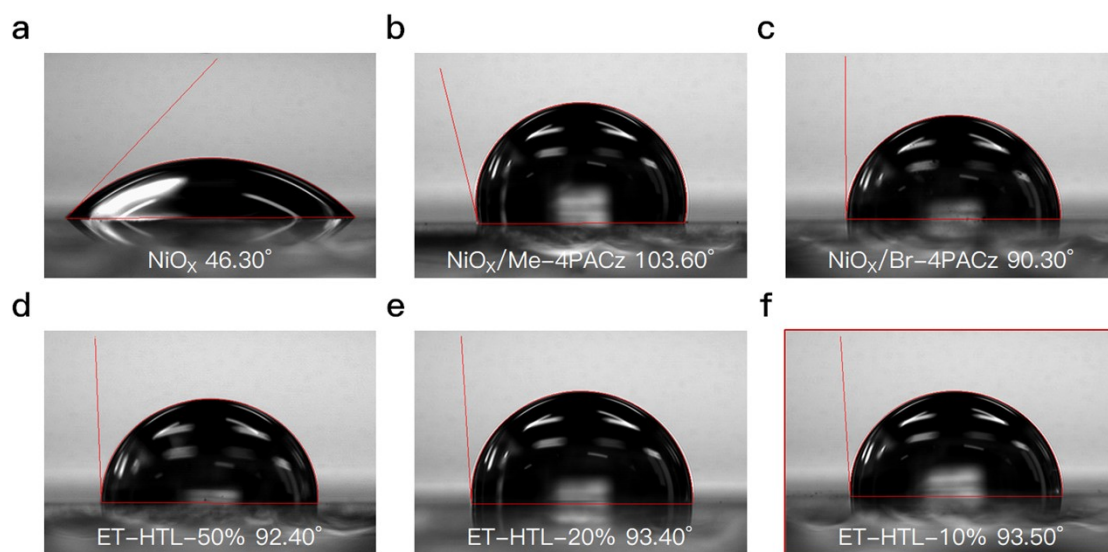


Figure S15. Water contact angle results of (a) bare NiO_x , (b) $\text{NiO}_x/\text{Me-4PACz}$, (c) $\text{NiO}_x/\text{Br-4PACz}$, (d) ET-HTL-50%, (e) ET-HTL-20% and (f) ET-HTL-10%.

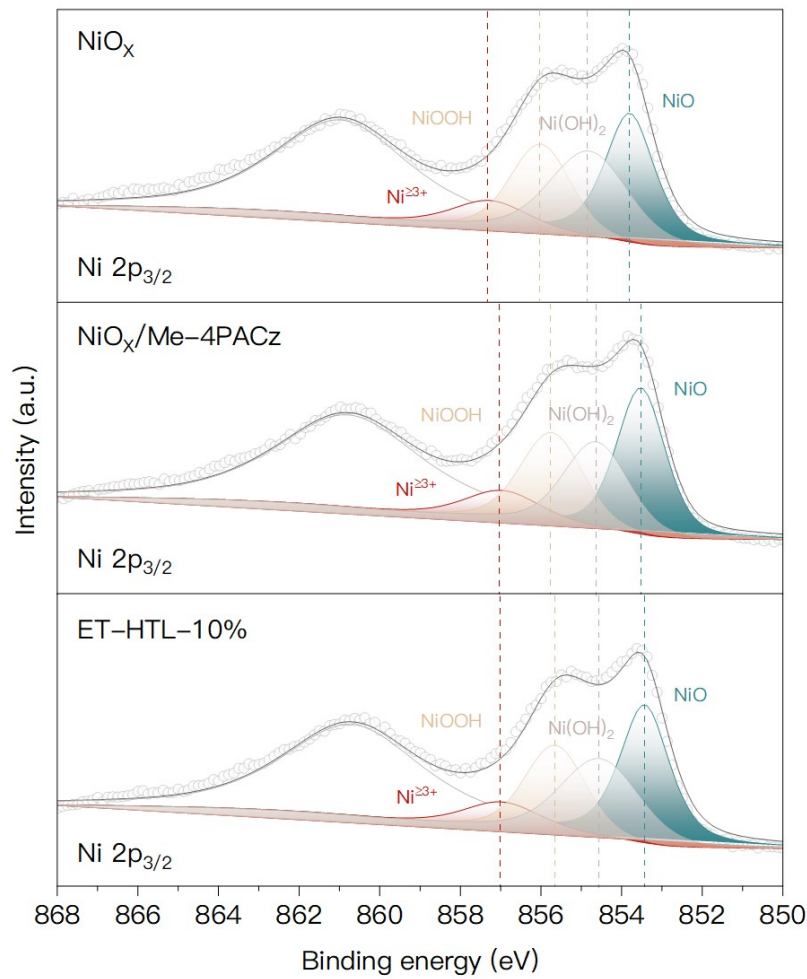


Figure S16. Ni $2p_{3/2}$ XPS spectra of bare NiO_x film, NiO_x/Me-4PACz and ET-HTL-10%. The results have been calibrated using standard carbon (C) peak (284.80 eV).

5 According to early researches, it is commonly accepted that the primary Ni^{≥3+} sites in all NiO_x function as a Brønsted-base that deprotonating the precursor amine, and as a Lewis acid that oxidizing I⁻, simultaneously, which creates defect on NiO_x/perovskite interface and leads to higher interface trap density, ultimately producing a severe efficiency loss.⁹ To investigate the role of bimolecular-SAM on NiO_x, XPS spectra of

10 NiO_x film. NiO_x/Me-4PACz and ET-HTL-10% film at the Ni core level were collected.

This analytical technique offered valuable insights into the changes in composition of NiO_x film, hence allowing for the verification of such changes.

According to the XPS studies reported previously, at least four unique species can be identified to gain a fitting of the Ni 2p spectral envelope, including NiO_x, Ni(OH)₂,
5 NiOOH, and Ni^{≥3+}.¹⁰⁻¹² **Table S1** provided a more intuitive presentation of the corresponding composition. After modified by Me-4PACz and bimolecular-SAM, there was a substantial shift in the peak of all species to a lower binding energy, showing successfully combination between phosphonic acid groups and Ni^{≥3+}. NiO_x/bimolecular-SAM facilitates the establishment of a more robust molecular
10 connection between phosphonic acid groups and Ni^{≥3+}, which effectively restrain the reactivity of active sites at the NiO_x/perovskite interface. Considering the detrimental effects of Ni^{≥3+} in the interaction with perovskite, this surface modification strategy presented a promising approach to enhance the efficiency and durability of PSCs.

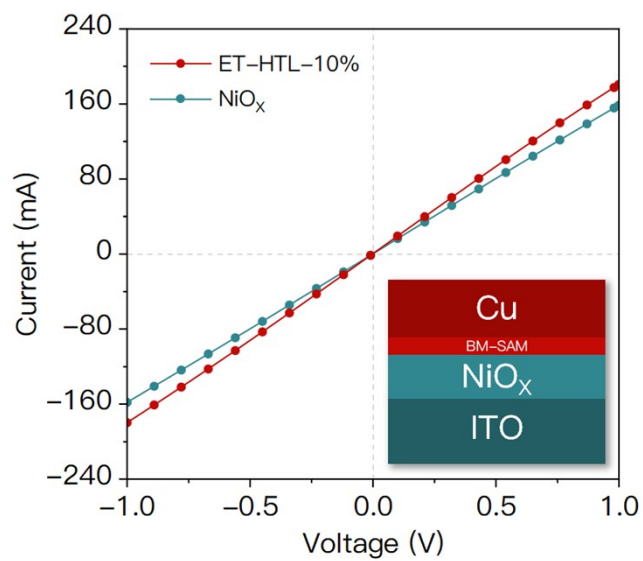


Figure S17. *I-V* curves of the devices with the structure of ITO/NiO_x/Cu and ITO/ET-HTL-10%/Cu for conductivity evaluation.

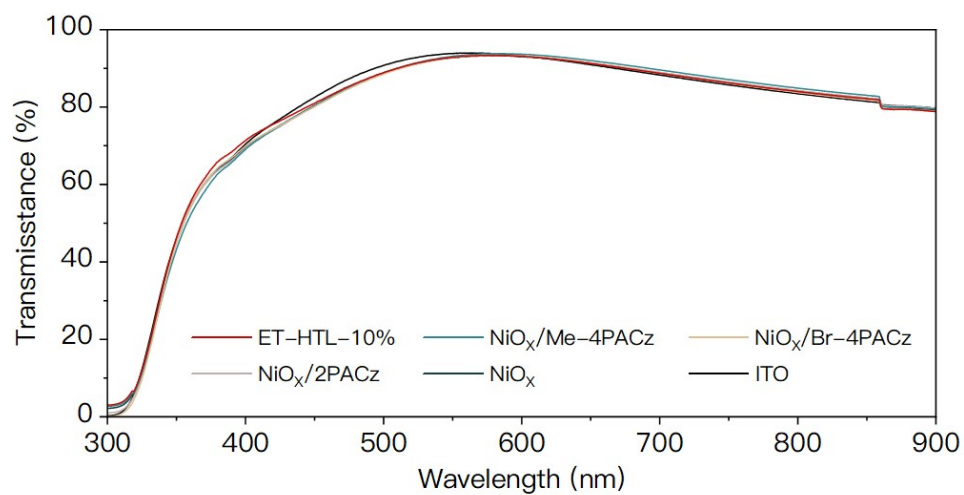


Figure S18. The UV transmittance spectra of ITO, bare NiO_x and NiO_x modified by different SAMs. The NiO_x was coated on ITO substrate and the testing background was set to be ambient air.

5

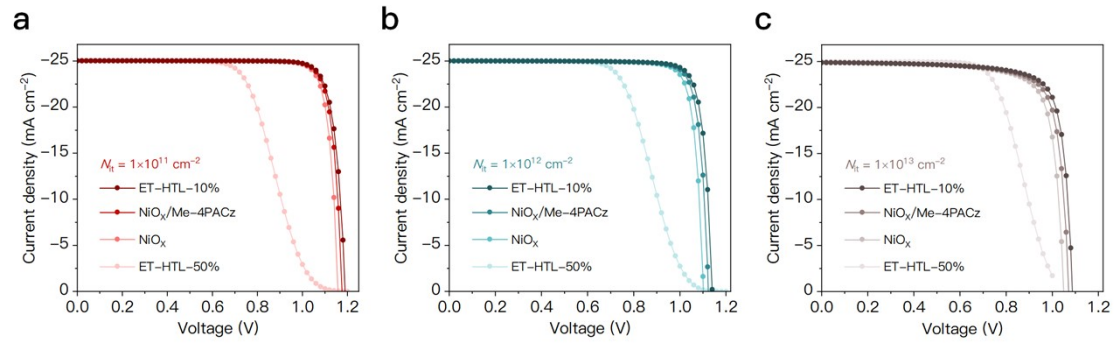


Figure S19. J - V curves of the designed structures with various HTLs under N_{it} levels of (a) $1 \times 10^{11} \text{ cm}^{-2}$, (b) $1 \times 10^{12} \text{ cm}^{-2}$ and (c) $1 \times 10^{13} \text{ cm}^{-2}$. The simulation measurement voltage was set from 0 V to 1.2 V.

5

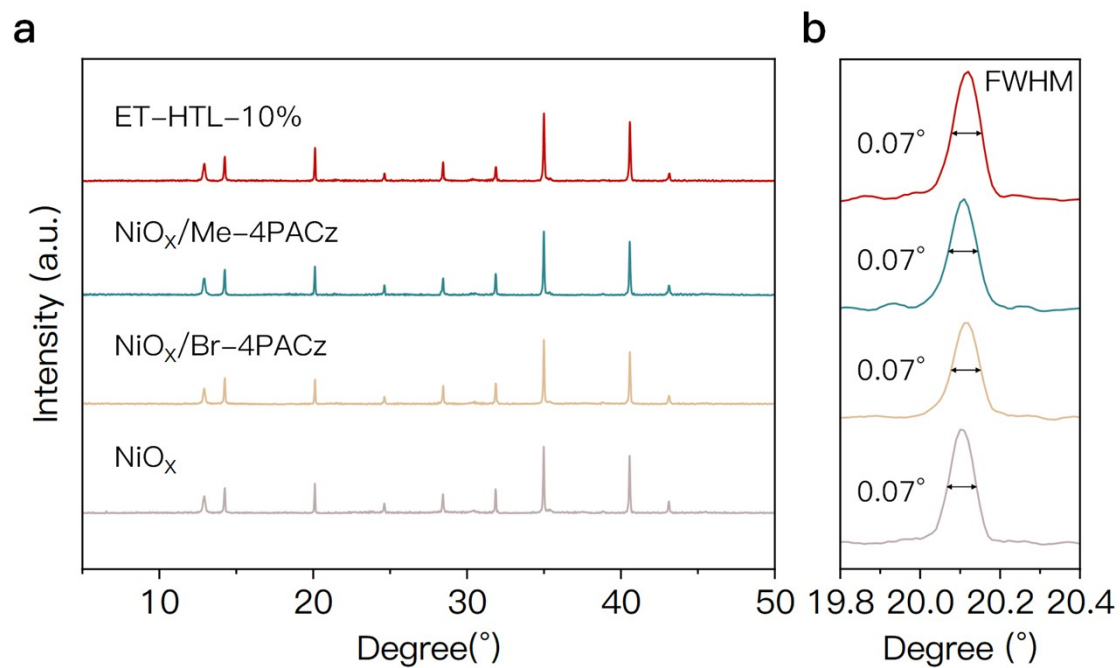


Figure S20. (a) XRD patterns of perovskite film coated on bare NiO_x, NiO_x/Me-4PACz, NiO_x/Br-4PACz and ET-HTL-10%. (b) Enlarged XRD patterns for full width at half maxima (FWHM) estimation.

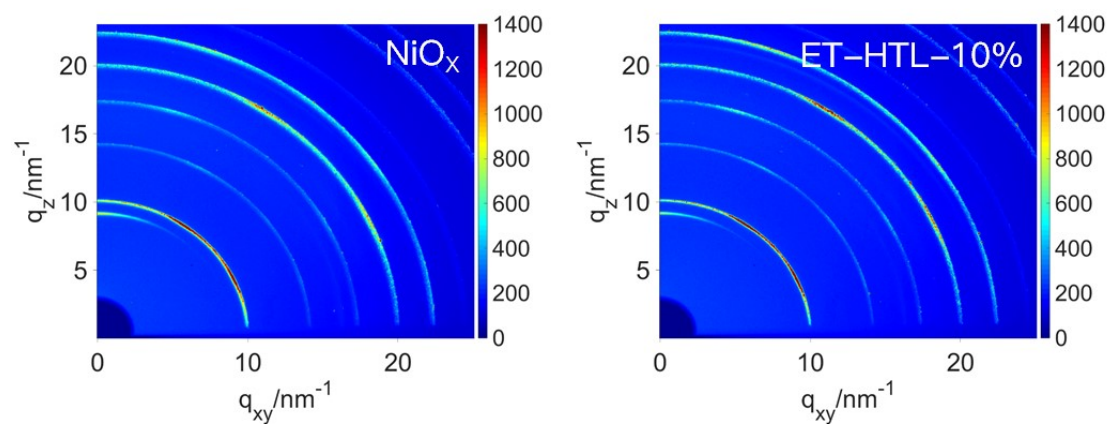


Figure S21. GIWAXS measurement results of perovskite films coated on bare NiO_x and ET-HTL-10%.

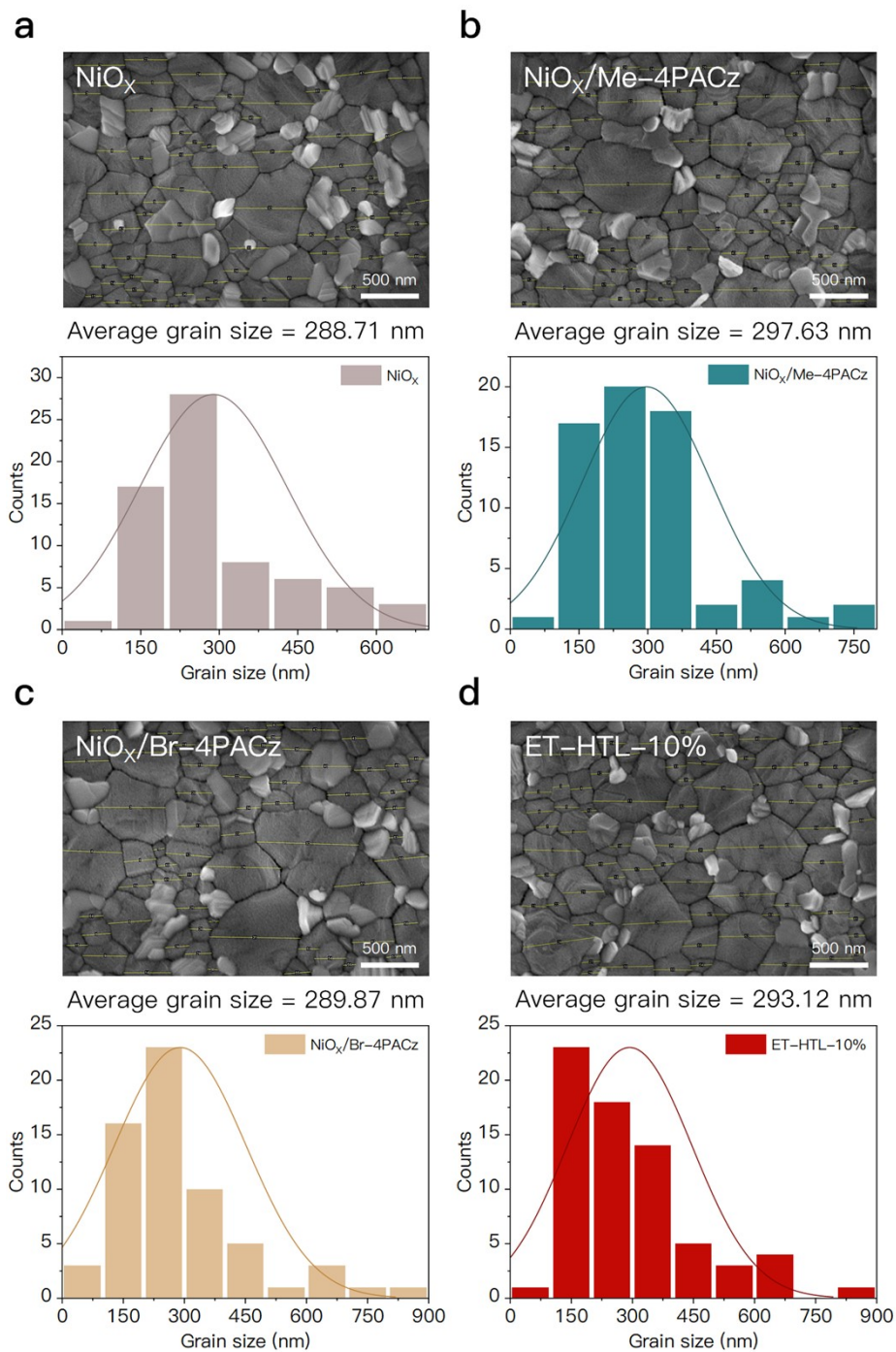


Figure S22. Statistical grain size analysis and corresponding grain size distribution of perovskite films deposited on (a) bare NiO_x , (b) $\text{NiO}_x/\text{Me-4PACz}$, (c) $\text{NiO}_x/\text{Br-4PACz}$ and (d) ET-HTL-10%. The fitting curves are the corresponding normal distribution curves. All tested films exhibited similar grain size with a fluctuation of less than 10 nm.

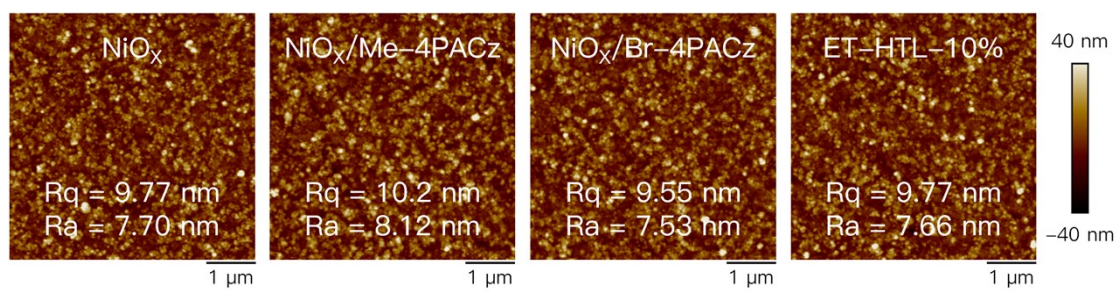


Figure S23. Corresponding AFM images measured using tapping mode on bare NiO_x,

NiO_x/Me-4PACz, NiO_x/Br-4PACz and ET-HTL-10%.

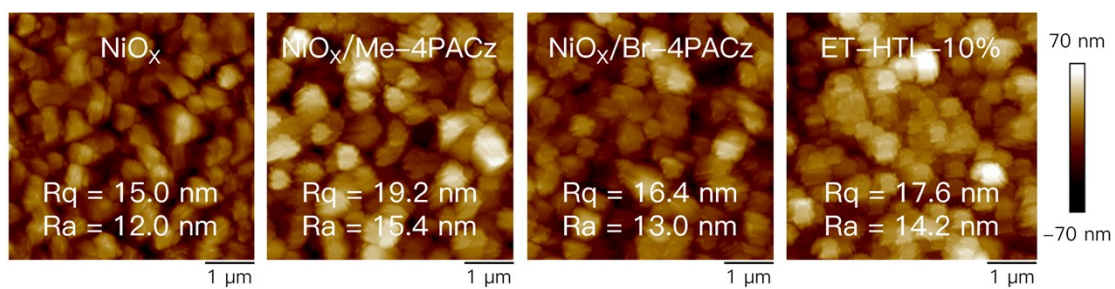


Figure S24. Corresponding AFM images measured using tapping mode on perovskite films coated on bare NiO_x, NiO_x/Me-4PACz, NiO_x/Br-4PACz and ET-HTL-10%.

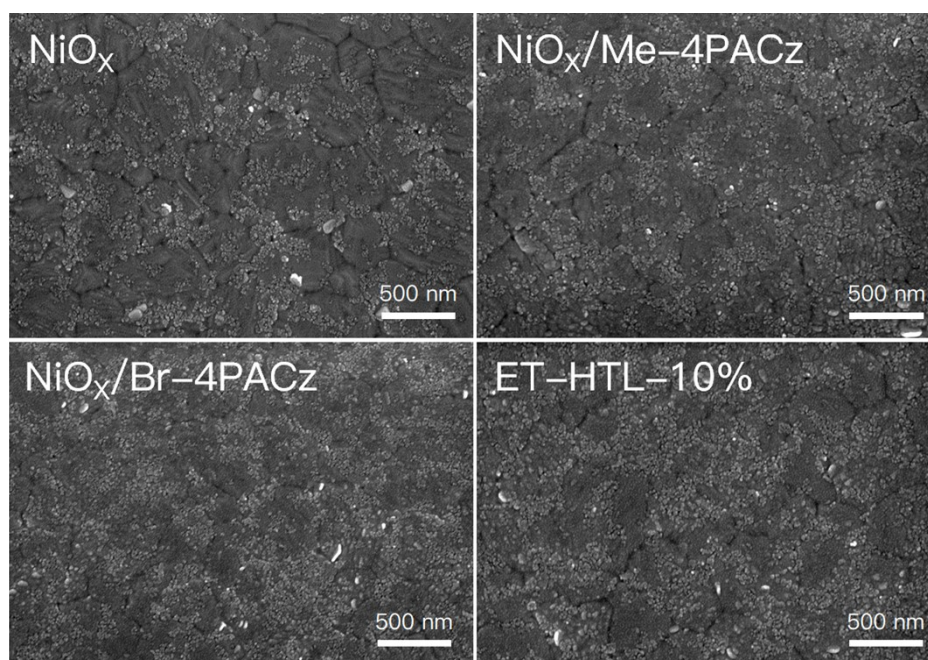


Figure S25. SEM images of the buried-side perovskite films coated on bare NiO_x, NiO_x/Me-4PACz, NiO_x/Br-4PACz and ET-HTL-10%. The perovskite films were peeled off using UV curing adhesive with a curing process involving irradiation with a 365 nm ultraviolet lamp for 5 min.

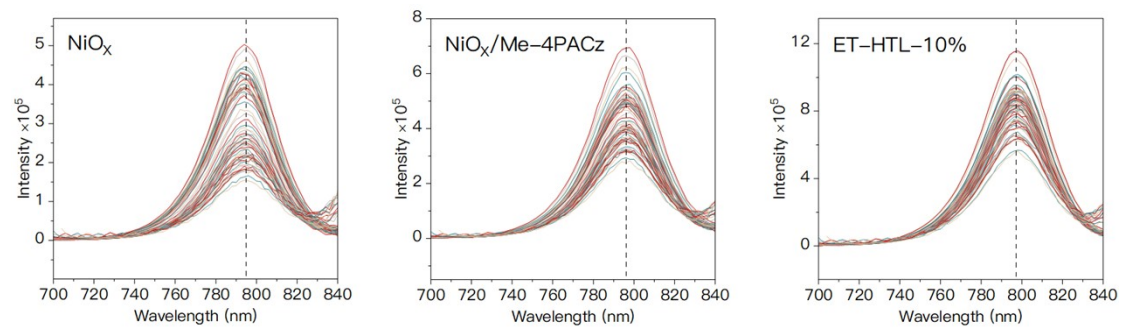


Figure S26. Raw data curves of EEM spectra with an excitation wavelength range from 350 to 700 nm of devices using bare NiO_x, NiO_x/Me-4PACz and ET-HTL-10%.

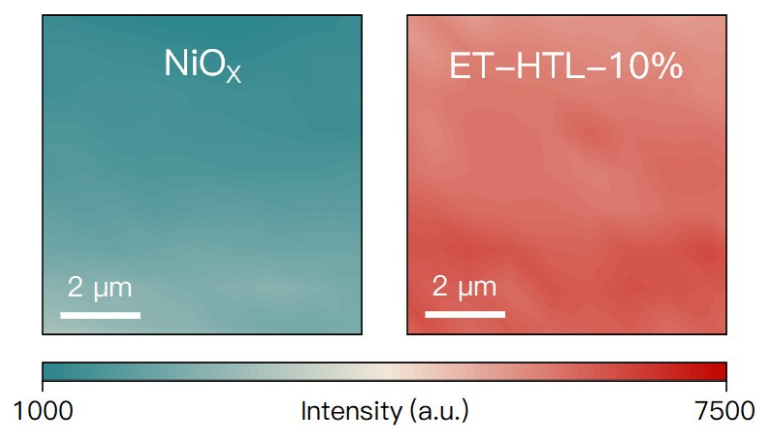


Figure S27. PL intensity mapping results of perovskite films coated on bare NiO_x and ET-HTL-10%. The PL spectra were taken from the bottom ITO side within 8 μm × 8 μm range.

5

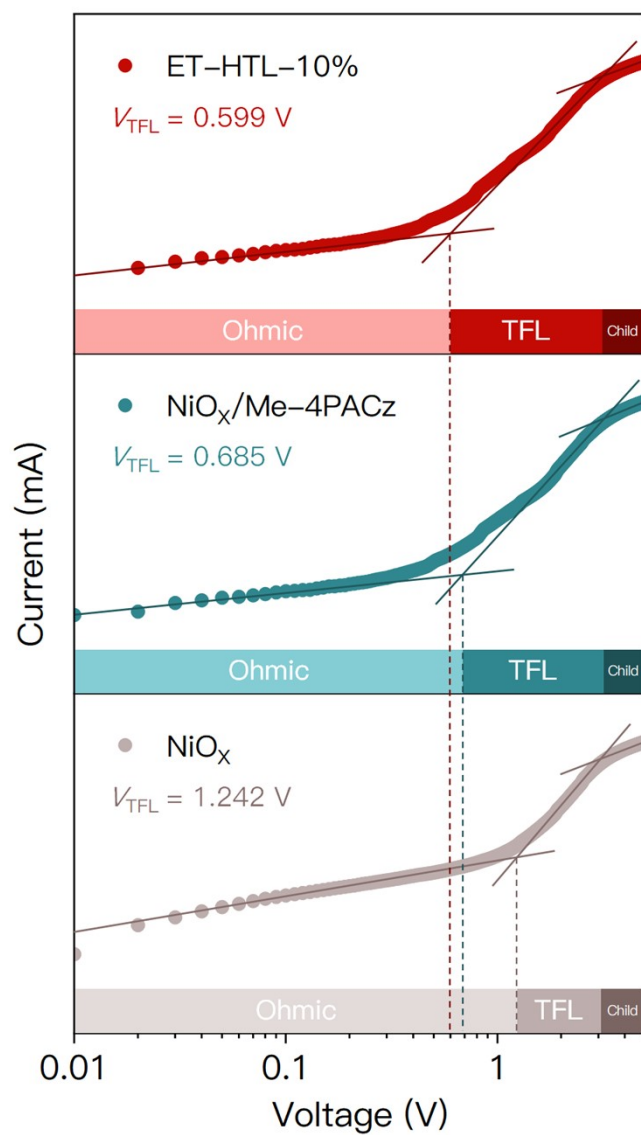


Figure S28. Dark I - V curves of hole-only structures (ITO/HTL/perovskite/PTAA/Au) with HTLs using bare NiO_x , $\text{NiO}_x/\text{Me-4PACz}$ and ET-HTL-10%, respectively.

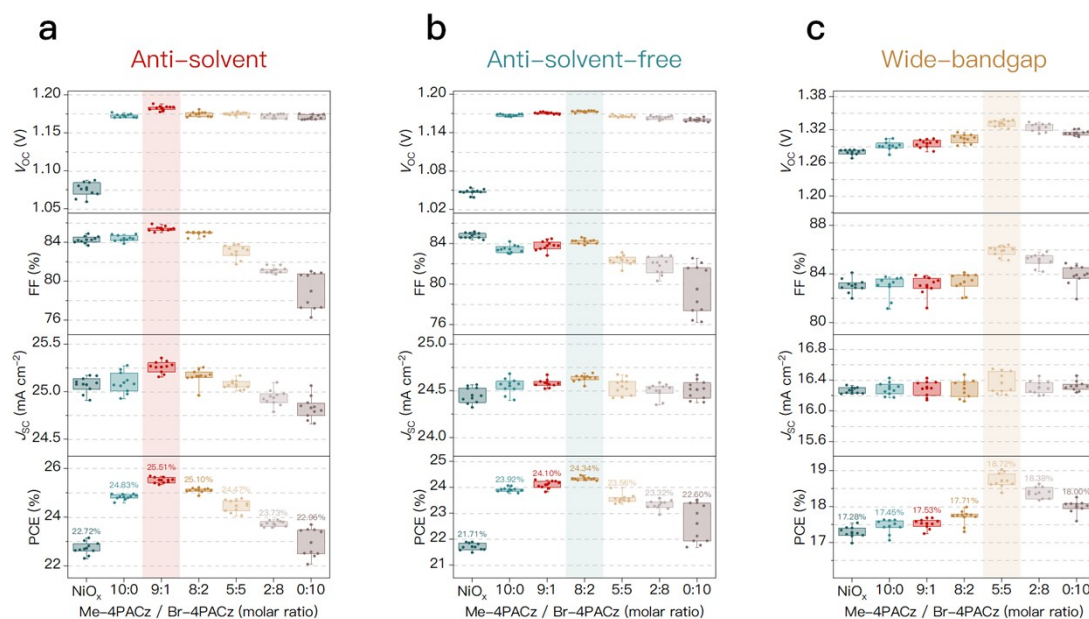


Figure S29. Performance comparison between inverted (a) anti-solvent PSCs, (b) anti-solvent-free PSCs and (c) wide-bandgap PSCs using bare NiO_x , $\text{NiO}_x/\text{Me-4PACz}$ (10:0), $\text{NiO}_x/\text{Br-4PACz}$ (0:10) and ET-HTLs with various bimolecular molar ratios 5 (Me-4PACz: Br-4PACz, 10 devices for each type). The point in the center of the box represents the mean value, the bounds of box indicate upper and lower quartiles, and the whiskers represent the minimum and maximum values.

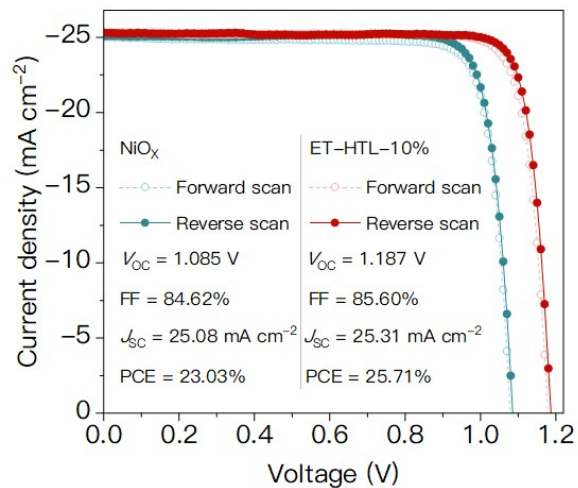


Figure S30. The champion J - V measurement results including forward scan and reverse scan of anti-solvent perovskite devices (0.0736 cm^2 active area) equipping bare NiO_x and ET-HTL-10% with ITO substrate.

5

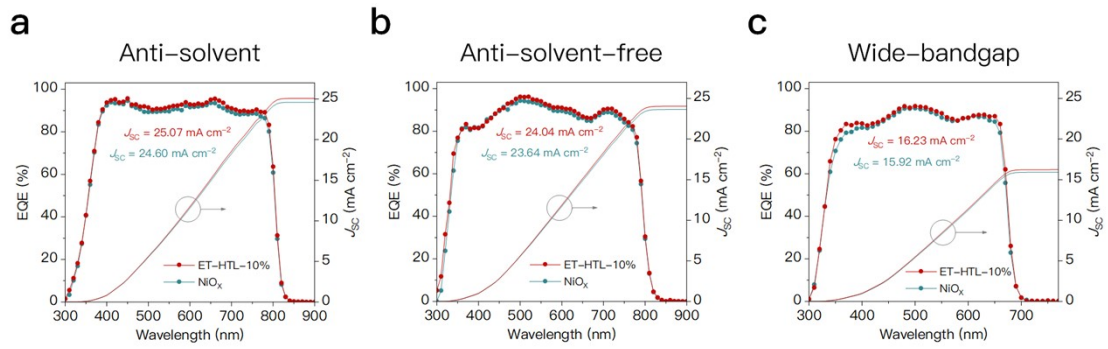


Figure S31. EQE spectra and integrated current density of the (a) champion anti-solvent PSCs equipping bare NiO_x and ET-HTL-10%, (b) champion anti-solvent-free PSCs equipping bare NiO_x and ET-HTL-20% and (c) champion wide-bandgap PSCs equipping bare NiO_x and ET-HTL-50% with ITO substrate. The J_{SC} obtained from EQE measurements and $J-V$ measurements exhibits a mismatch within 5%.

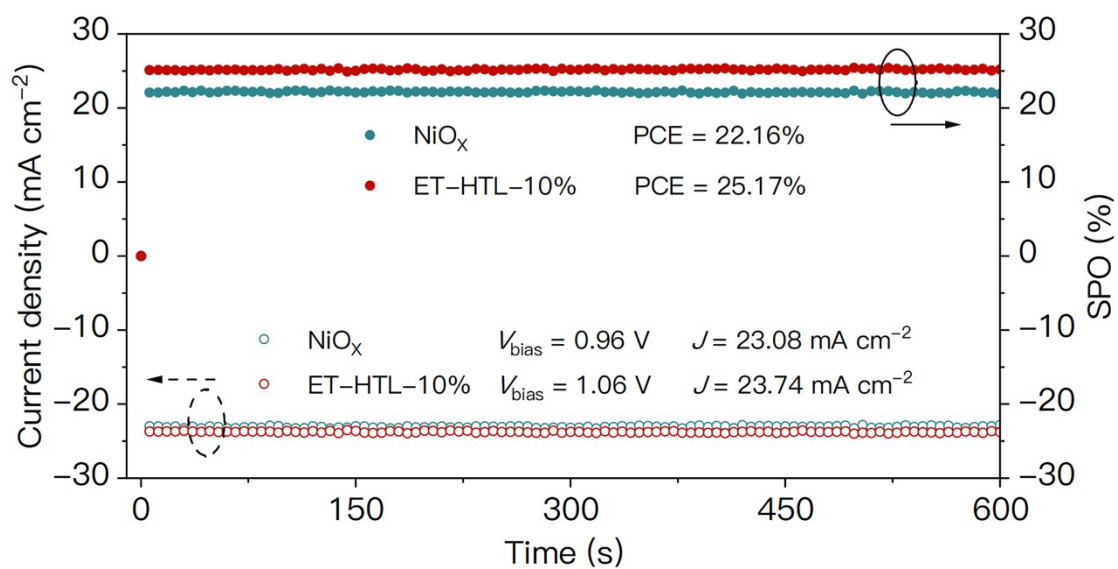


Figure S32. Steady power output (SPO) for 600 seconds of unencapsulated inverted PSCs equipping bare NiO_x and ET-HTL-10% with ITO substrate in N₂ atmosphere at room temperature under 1 sun continuous illumination.

5

Measurement Report

Report No. 23TR120707

Client Name Baomin Xu's Group, Southern University of Science and Technology
Client Address No.1088, Xueyuan Avenue, Nanshan District, Shenzhen, China
Sample Inverted Perovskite Photovoltaic Cell
Manufacturer Baomin Xu's Group, Southern University of Science and Technology
Measurement Date 7th December, 2023

Performed by: Qiang Shi *Qiang Shi* **Date:** 07/12/2023
Reviewed by: Wenjie Zhao *Wenjie Zhao* **Date:** 07/12/2023
Approved by: Yucheng Liu *Yucheng Liu* **Date:** 07/12/2023

Address: No.235 Chengbei Road, Jiading, Shanghai **Post Code:** 201800
E-mail: solarcell@mail.sim.ac.cn **Tel:** +86-021-69976921

The measurement report without signature and seal are not valid.
 This report shall not be reproduced, except in full, without the approval of SIMIT.



Report No. 23TR120707

====Measurement Results====

	Forward Scan (Isc to Voc)	Reverse Scan (Voc to Isc)
Area	6.76 mm ²	
Isc	1.733 mA	1.741 mA
Voc	1.181 V	1.179 V
Pmax	1.680 mW	1.744 mW
Ipm	1.634 mA	1.678 mA
Vpm	1.028 V	1.039 V
FF	82.08 %	84.97 %
Eff	24.85 %	25.80 %

- Spectral Mismatch Factor: SMM=0.9940.
- Designated illumination area defined by a thin mask was measured by measuring microscope.
- Test results listed in this measurement report refer exclusively to the mentioned measured sample.
- The results apply only at the time of the test, and do not imply future performance.

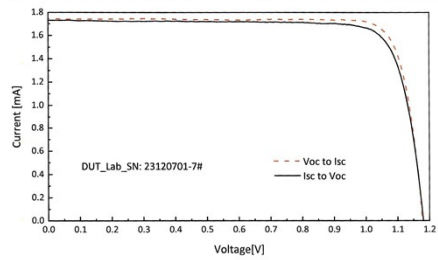


Fig.1 I-V curves of the measured sample

-----End of Report-----

Figure S33. The certification result for inverted PSC (0.0676 cm² aperture area) based on ET-HTL-10% measured by Shanghai Institute of Microsystem and Information Technology (SIMIT). The device shows a PCE of 25.80% under the reverse *J-V* scan (V_{OC} = 1.179 V, FF = 84.97% and J_{SC} = 25.75 mA cm⁻²).

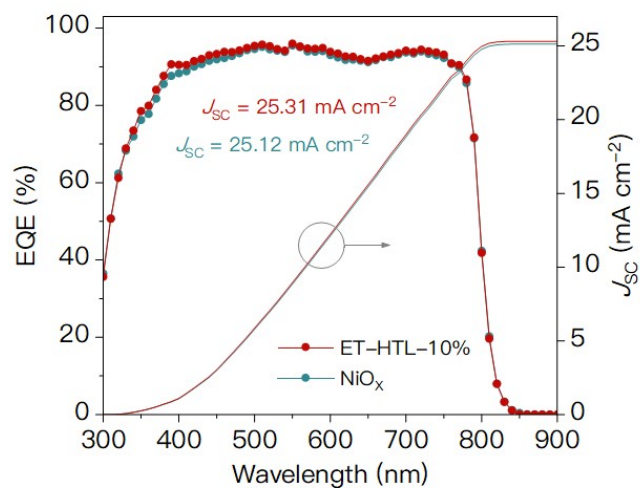


Figure S34. EQE spectra and integrated current density of the champion PSCs equipping bare NiO_x and ET-HTL-10% with FTO substrate. The J_{SC} obtained from EQE measurements and $J-V$ measurements exhibits a mismatch within 2%.

5

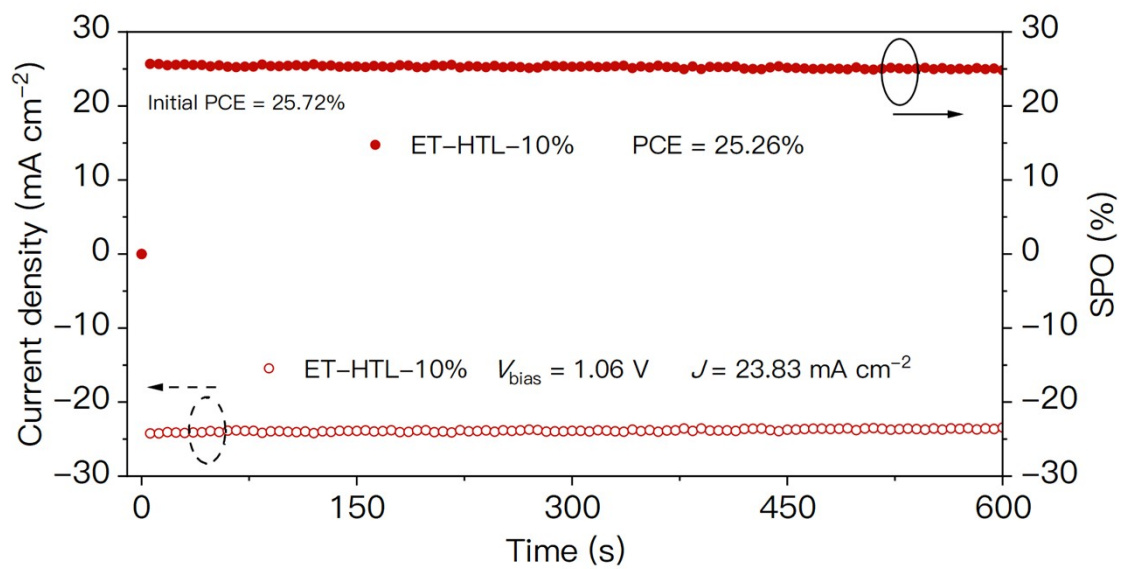


Figure S35. Steady power output (SPO) for 600 seconds of the champion unencapsulated inverted PSCs equipping ET-HTL-10% with FTO substrate in N₂ atmosphere at room temperature under 1 sun continuous illumination.

5

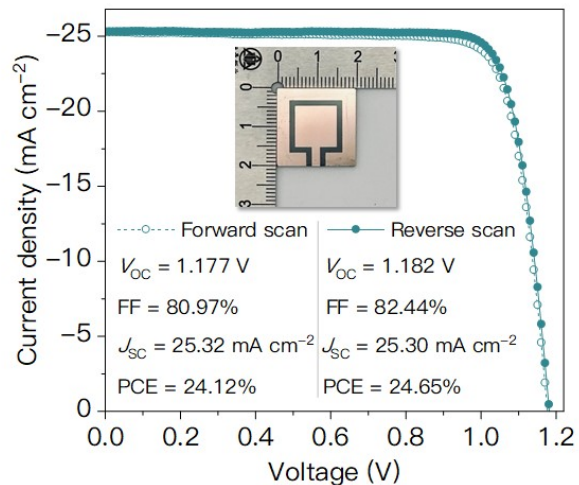


Figure S36. The device performance and the champion $J-V$ measurement results including forward scan and reverse scan of large-area anti-solvent perovskite devices (1.1 cm² active area) equipping ET-HTL-10% with ITO substrate.

5

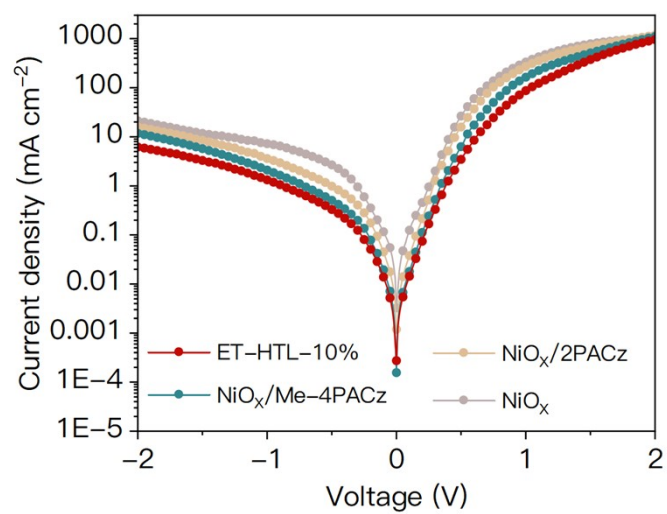


Figure S37. Dark J - V measurement results of PSCs with bare NiO_x, NiO_x/2PACz, NiO_x/Me-4PACz and ET-HTL-10%.

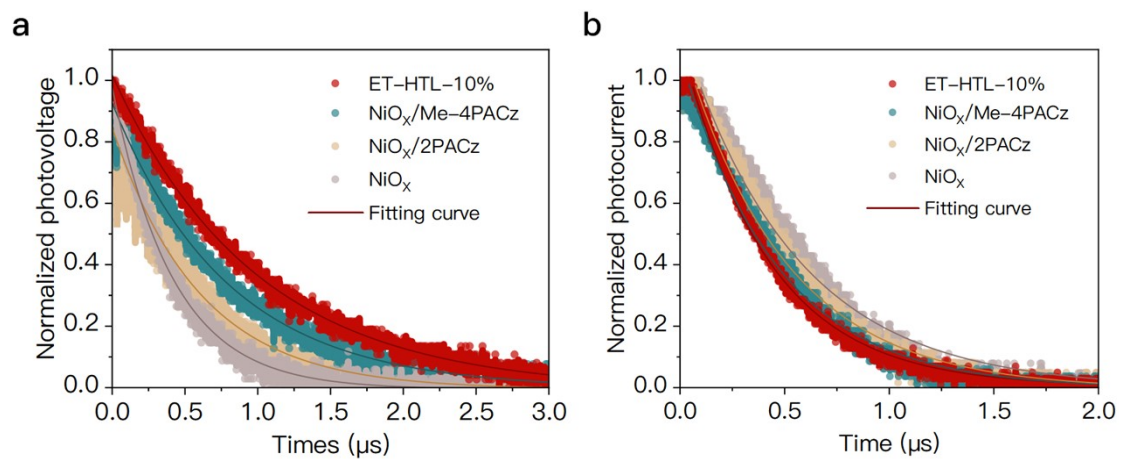


Figure S38. (a) TPV and (b) TPC measurements and corresponding fitting results of devices with bare NiO_x , $\text{NiO}_x/2\text{PACz}$, $\text{NiO}_x/\text{Me-4PACz}$ and ET-HTL-10%.

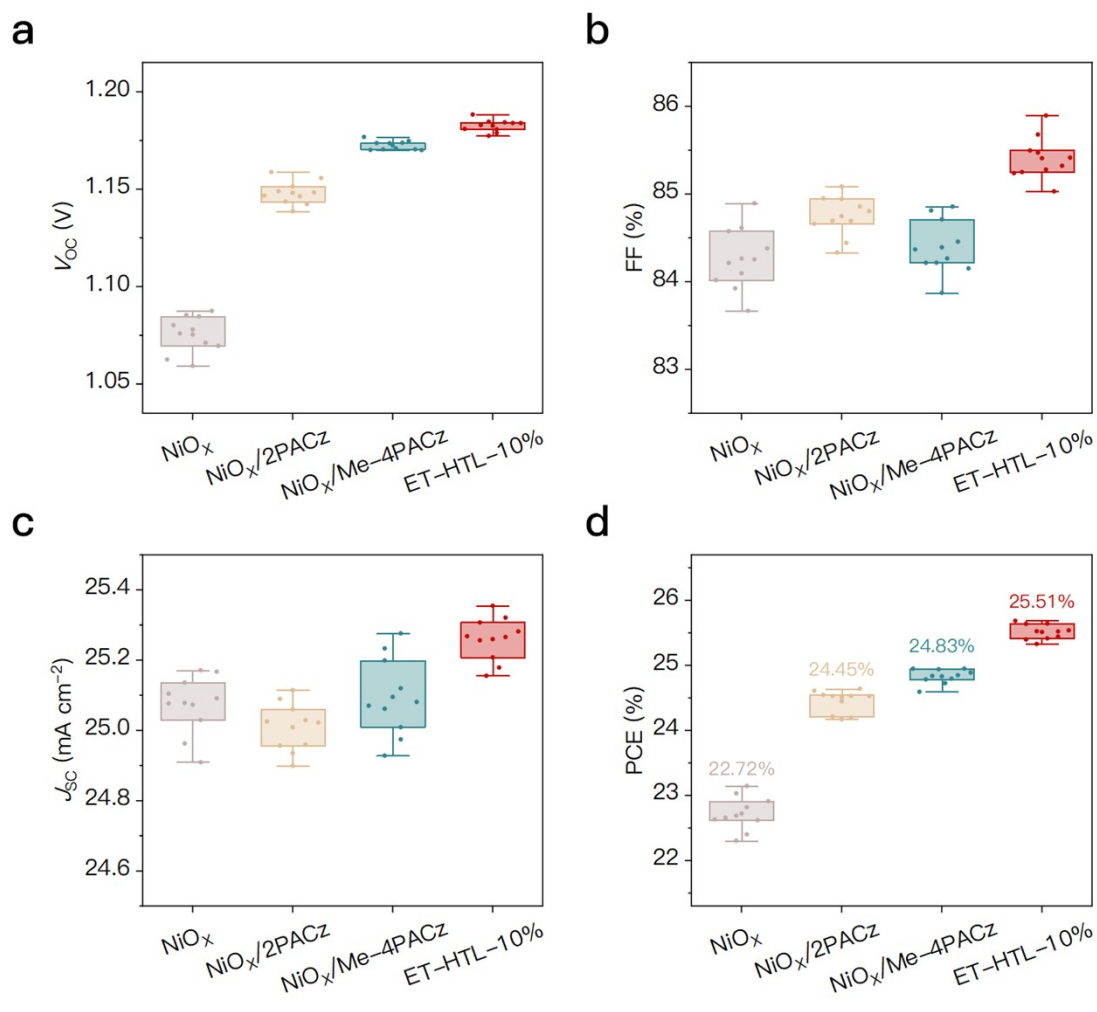


Figure S39. Performance comparison between inverted PSCs using bare NiO_x, NiO_x/2PACz, NiO_x/Me-4PACz and ET-HTL-10% (10 devices for each type). The point in the center of the box represents the mean value, the bounds of box indicate 5 upper and lower quartiles, and the whiskers represent the minimum and maximum values.

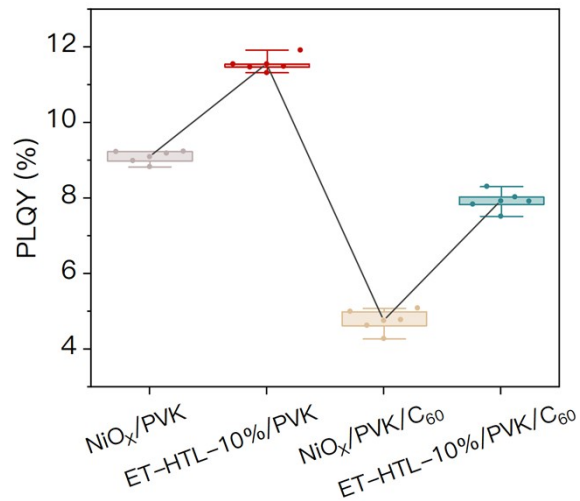


Figure S40. PLQY measurement results of different HTL/perovskite and HTL/perovskite/ETL junctions (5 samples for each type). The center point represents the mean value, the bounds of box indicate upper and lower quartiles and the whiskers represent the minimum and maximum values.

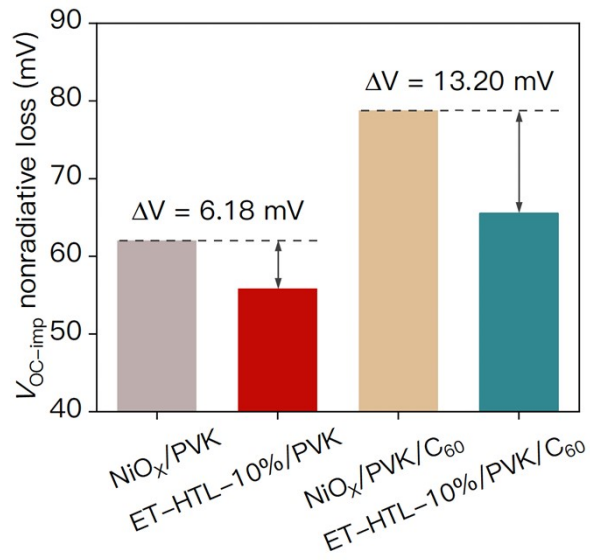


Figure S41. The V_{oc-imp} nonradiative recombination loss of corresponding HTL/perovskite and HTL/perovskite/ETL junctions.

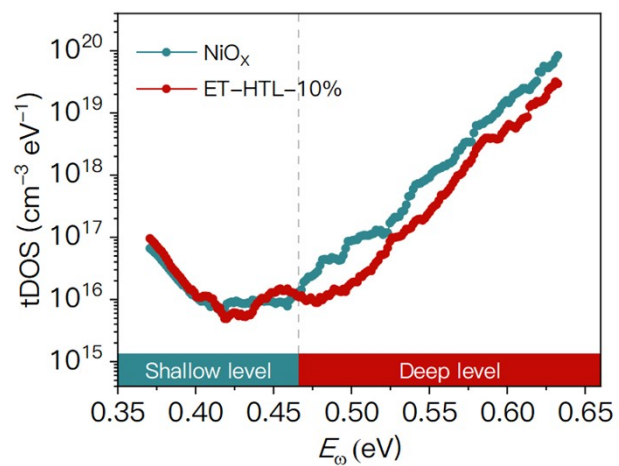


Figure S42. tDOS calculation results of devices with bare NiO_x and ET-HTL-10%.

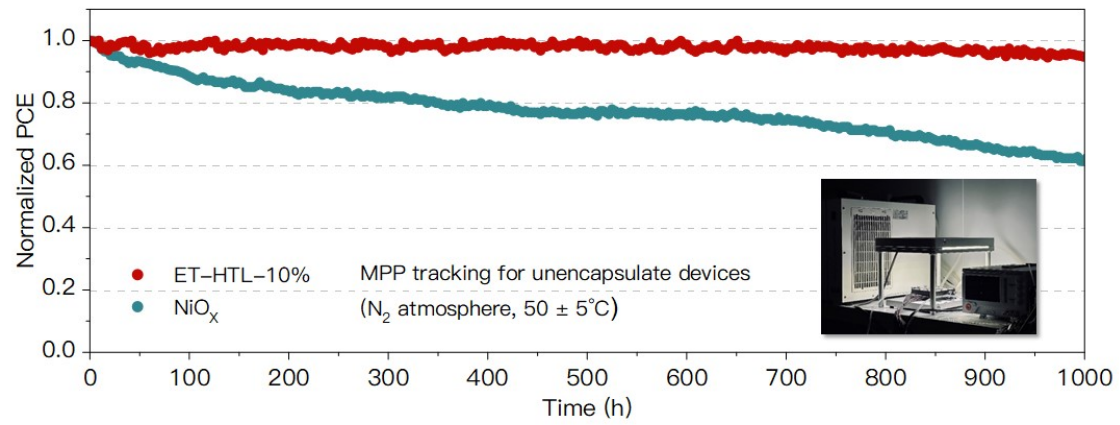


Figure S43. Normalized PCE evolution of devices with bare NiO_x and ET-HTL-10% at the MPP under continuous illumination in nitrogen.

Table S1. Binding energy of various species in NiO_x according to peak fitting of the Ni 2p_{3/2} core level spectra.

Samples	NiO	NiOOH	Ni(OH) ₂	Ni ^{≥3+}	Composite 1	Composite 2
NiO _x	853.81	856.03	854.85	857.32	853.97	855.76
NiO _x / Me-4PACz	853.52	855.76	854.64	857.04	853.70	855.41
ET-HTL- 10%	853.44	855.66	854.56	857.02	853.56	855.37

Table S2. Working point parameters used for simulation in SCAPS-1D.

Temperature (k)	Voltage (V)	Frequency (Hz)	Number of
300	0	1×10^6	5

Table S3. Relevant parameters used for simulation in SCAPS-1D.

Parameter	NiO _x	SAM	Perovskite	C ₆₀
Thickness (nm)	20	5	750	30
Bandgap (eV)	3.6	3.6	1.56	1.9
Electron affinity (eV)	1.75	1.79/1.87/2.15/2.48	3.92	3.9
Dielectric permittivity (relative)	11.750	11.750	31	4.2
CB effective density of states (cm ⁻³)	2.5×10 ²⁰	2.5×10 ²⁰	2×10 ¹⁸	8×10 ¹⁹
VB effective density of states (cm ⁻³)	2.5×10 ²⁰	2.5×10 ²⁰	1.8×10 ¹⁹	8×10 ¹⁹
Electron thermal velocity (cm/s)	1×10 ⁷	1×10 ⁷	1×10 ⁷	1×10 ⁷
Hole thermal velocity (cm/s)	1×10 ⁷	1×10 ⁷	1×10 ⁷	1×10 ⁷
Electron mobility (cm ² /Vs)	1×10 ⁻³	1×10 ⁻³	0	1×10 ⁻²
Hole mobility (cm ² /Vs)	1×10 ⁻³	1×10 ⁻³	0	1×10 ⁻⁵
Shallow uniform donor density N_D (cm ⁻³)	0	0	1×10 ¹²	1×10 ¹⁸
Shallow uniform	1×10 ¹⁸	1×10 ¹⁸	1×10 ¹⁴	0

acceptor density N_A (cm⁻³)

Radiative recombination

coefficient C_{Rad} (cm³ s⁻¹) 0 0 1×10^{-12} 0

Auger electron capture

coefficient A_n (cm⁶ s⁻¹) 0 0 2.3×10^{-29} 0

Auger hole capture

coefficient A_p (cm⁶ s⁻¹) 0 0 2.3×10^{-29} 0

Table S4. Relevant defect parameters used for simulation in SCAPS-1D.

Defect parameter	NiO_x	SAM/Perovskite	Perovskite	C₆₀
Defect type	Neutral	Neutral	Single acceptor	Neutral
Capture cross section (electrons) (cm⁻³)	2×10^{-14}	1×10^{-17}	1×10^{-15}	2×10^{-14}
Capture cross section (hole) (cm⁻³)	2×10^{-14}	1×10^{-17}	1×10^{-15}	2×10^{-14}
Energetic distribution	Gaussian	Gaussian	Single	Gaussian
Energy level (eV)	0.6	0.6	0.3	0.6
Characteristic energy (eV)	0.1	0.1	None	0.1
Total defect density (cm⁻³)	1×10^{14}	Variable	5×10^{13}	1×10^{14}
Peak defect density (cm⁻³)	5.642×10^{14}	Variable	None	5.642×10^{14}

Table S5. The TRPL fitting results of perovskite films coated on NiO_x, NiO_x/Me-4PACz and ET-HTL-10%.

Samples	A_1	τ_1 (ns)	A_2	τ_2 (ns)	τ_{avg} (ns)
NiO _x	614.92	111.77	608.23	516.02	443.40
NiO _x /Me-4PACz	449.45	89.61	801.47	1360.99	1315.72
ET-HTL-10%	539.98	73.54	888.63	1538.26	1496.91

Table S6. Performance summary of champion PSCs with different perovskites coated on NiO_x and ET-HTLs. All parameters are extracted from J - V measurements in **Figures 4c to e**, including forward scan and reverse scan.

Perovskite	Sample	Scan direction	V_{OC} (V)	FF (%)	J_{SC} (mA cm ⁻²)	PCE (%)
Anti-solvent (ITO substrate)	NiO _x	Forward	1.079	83.75	25.04	22.62
		Reverse	1.085	84.62	25.08	23.03
	ET-HTL- 10%	Forward	1.178	84.53	25.32	25.22
		Reverse	1.187	85.60	25.31	25.71
Anti-solvent (FTO substrate)	NiO _x	Forward	1.061	85.49	25.57	23.19
		Reverse	1.063	85.71	25.59	23.32
	ET-HTL- 10%	Forward	1.184	84.32	25.71	25.66
		Reverse	1.187	85.82	25.79	26.28
Anti-solvent-free	NiO _x	Forward	1.047	84.59	24.41	21.61
		Reverse	1.054	84.58	24.55	21.89
	ET-HTL- 20%	Forward	1.168	84.18	24.58	24.17
		Reverse	1.173	84.50	24.66	24.44
Wide-bandgap	NiO _x	Forward	1.281	82.89	16.28	17.28
		Reverse	1.280	84.11	16.29	17.54
	ET-HTL- 50%	Forward	1.330	86.07	16.48	18.87
		Reverse	1.339	86.39	16.46	19.03

Table S7. The TPV fitting results of device with NiO_x, NiO_x/2PACz, NiO_x/Me-4PACz and ET-HTL-10%.

Samples	A_1	τ_1 (μs)
NiO _x	0.98	0.416
NiO _x /2PACz	0.85	0.601
NiO _x /Me-4PACz	0.93	0.794
ET-HTL-10%	1.02	0.988

Table S8. The TPC fitting results of device with NiO_x, NiO_x/2PACz, NiO_x/Me-4PACz and ET-HTL-10%.

Samples	A_1	τ_1 (μs)
NiO _x	1.17	0.547
NiO _x /2PACz	1.15	0.495
NiO _x /Me-4PACz	1.09	0.462
ET-HTL-10%	1.13	0.417

Table S9. The PLQY, QFLS and $\Delta V_{OC-imp}^{nonrad}$ values of different perovskite junctions.

Junctions	PLQY (%)	QFLS (eV)	$\Delta V_{OC-imp}^{nonrad}$ (mV)
NiO _x /perovskite	9.10	1.19723	61.98
ET-HTL-10%/perovskite	11.55	1.19949	55.80
NiO _x /perovskite/C ₆₀	4.76	1.18047	78.74
ET-HTL-10%/perovskite/C ₆₀	7.92	1.18975	65.54

Supplementary References

1. P. Zhu, S. Gu, X. Luo, Y. Gao, S. Li, J. Zhu and H. Tan, *Advanced Energy Materials*, 2020, **10**, 1903083.
2. G. Kresse and J. Furthmüller, *Physical Review B*, 1996, **54**, 11169-11186.
- 5 3. S. L. Dudarev, G. A. Botton, S. Y. Savrasov, C. J. Humphreys and A. P. Sutton, *Physical Review B*, 1998, **57**, 1505-1509.
4. M. Burgelman, P. Nollet and S. Degraeve, *Thin Solid Films*, 2000, **361-362**, 527-532.
5. R. Kotipalli, O. Poncelet, G. Li, Y. Zeng, L. A. Francis, B. Vermang and D.
10 Flandre, *Solar Energy*, 2017, **157**, 603-613.
6. Y. Yang, S. Cheng, X. Zhu, S. Li, Z. Zheng, K. Zhao, L. Ji, R. Li, Y. Liu, C. Liu, Q. Lin, N. Yan and Z. Wang, *Nature Energy*, 2024, **9**, 37-46.
7. P. Caprioglio, M. Stolterfoht, C. M. Wolff, T. Unold, B. Rech, S. Albrecht and D. Neher, *Advanced Energy Materials*, 2019, **9**, 1901631.
- 15 8. L. Li, Y. Wang, X. Wang, R. Lin, X. Luo, Z. Liu, K. Zhou, S. Xiong, Q. Bao, G. Chen, Y. Tian, Y. Deng, K. Xiao, J. Wu, M. I. Saidaminov, H. Lin, C.-Q. Ma, Z. Zhao, Y. Wu, L. Zhang and H. Tan, *Nature Energy*, 2022, **7**, 708-717.
9. C. C. Boyd, R. C. Shallcross, T. Moot, R. Kerner, L. Bertoluzzi, A. Onno, S. Kavadiya, C. Chosy, E. J. Wolf, J. Werner, J. A. Raiford, C. de Paula, A. F.
20 Palmstrom, Z. J. Yu, J. J. Berry, S. F. Bent, Z. C. Holman, J. M. Luther, E. L. Ratcliff, N. R. Armstrong and M. D. McGehee, *Joule*, 2020, **4**, 1759-1775.
10. N. Weidler, J. Schuch, F. Knaus, P. Stenner, S. Hoch, A. Maljusch, R. Schäfer, B. Kaiser and W. Jaegermann, *The Journal of Physical Chemistry C*, 2017, **121**, 6455-6463.
- 25 11. G. Qu, D. Wang, X. Liu, Y. Qiao, D. Khan, Y. Li, J. Zeng, P. Xie, Y. Xu, P. Zhu, L. Huang, Y.-G. Wang, B. Xu and Z.-X. Xu, *Journal of Energy Chemistry*, 2023, **85**, 39-48.
12. Z. Jiang, D. Wang, J. Sun, B. Hu, L. Zhang, X. Zhou, J. Wu, H. Hu, J. Zhang, W. C. H. Choy and B. Xu, *Small Methods*, 2024, **8**, 2300241.